NAVAL POSTGRADUATE SCHOOL

MONTEREY, CALIFORNIA

THESIS

NEUTRALLY BUOYANT BIOMIMETIC DIRECTIONAL MEMS SENSOR

by

Leland McCarty

December 2020

Thesis Advisor: Fabio D. Durante Pereira Alves
Co-Advisor: Gamani Karunasiri

THIS PAGE INTENTIONALLY LEFT BLANK

REPORT DOCUMENTATION PAGE			*Form Approved OMB No. 0704-0188*

1. AGENCY USE ONLY *(Leave blank)*	**2. REPORT DATE** December 2020	**3. REPORT TYPE AND DATES COVERED** Master's thesis

4. TITLE AND SUBTITLE NEUTRALLY BUOYANT BIOMIMETIC DIRECTIONAL MEMS SENSOR	**5. FUNDING NUMBERS** RPNVM
6. AUTHOR(S) Leland McCarty	
7. PERFORMING ORGANIZATION NAME(S) AND ADDRESS(ES) Naval Postgraduate School Monterey, CA 93943-5000	**8. PERFORMING ORGANIZATION REPORT NUMBER**
9. SPONSORING / MONITORING AGENCY NAME(S) AND ADDRESS(ES) ONR - Arlington, VA 22203	**10. SPONSORING / MONITORING AGENCY REPORT NUMBER**

11. SUPPLEMENTARY NOTES The views expressed in this thesis are those of the author and do not reflect the official policy or position of the Department of Defense or the U.S. Government.

12a. DISTRIBUTION / AVAILABILITY STATEMENT Approved for public release. Distribution is unlimited.	**12b. DISTRIBUTION CODE** A

13. ABSTRACT (maximum 200 words)

This thesis presents an analysis of a unique Micro Electrical Mechanical System (MEMS) sensor adapted for underwater sound detection and localization. The sensor is inspired by the hearing system of the *Ormia ochracea* parasitoid fly and is being investigated to serve as a miniature replacement, or supplement, to traditional underwater sound detection systems such as hydrophones and hydrophone arrays. The sensor operates at its resonant frequency as a single-axis, in-plane, capacitive sensing accelerometer with two mechanically coupled sensing elements, and it possesses inherently dipole directionality. The mechanisms for sound detection using this sensor are discussed, and an engineering approach to underwater sound detection in a neutrally buoyant configuration is demonstrated. The sensitivity of the sensor was 0.81 V/mg (-131.9 dB re 1V/μPa), and its noise spectral density was 95 $\mu V/\sqrt{Hz}$. Cross-axial sensitivity was -13 dB. Measurements verified that the sensor's characteristics operating in air did not change while operating underwater in a neutrally buoyant configuration.

14. SUBJECT TERMS mems, acoustics, acoustic sensor, sensors, microphones, inertial sensor, accelerometer, underwater, neutrally buoyant, vector sensor, biomimetic	**15. NUMBER OF PAGES** 103
	16. PRICE CODE

17. SECURITY CLASSIFICATION OF REPORT	**18. SECURITY CLASSIFICATION OF THIS PAGE**	**19. SECURITY CLASSIFICATION OF ABSTRACT**	**20. LIMITATION OF ABSTRACT**
Unclassified	Unclassified	Unclassified	UU

NSN 7540-01-280-5500 Standard Form 298 (Rev. 2-89)
Prescribed by ANSI Std. 239-18

THIS PAGE INTENTIONALLY LEFT BLANK

Approved for public release. Distribution is unlimited.

NEUTRALLY BUOYANT BIOMIMETIC DIRECTIONAL MEMS SENSOR

Leland McCarty
Lieutenant Commander, United States Navy
BS, University of California, San Diego, 2010

Submitted in partial fulfillment of the
requirements for the degree of

MASTER OF SCIENCE IN APPLIED PHYSICS

from the

NAVAL POSTGRADUATE SCHOOL
December 2020

Approved by: Fabio D. Durante Pereira Alves
Advisor

Gamani Karunasiri
Co-Advisor

Kevin B. Smith
Chair, Department of Physics

THIS PAGE INTENTIONALLY LEFT BLANK

ABSTRACT

This thesis presents an analysis of a unique Micro Electrical Mechanical System (MEMS) sensor adapted for underwater sound detection and localization. The sensor is inspired by the hearing system of the *Ormia ochracea* parasitoid fly and is being investigated to serve as a miniature replacement, or supplement, to traditional underwater sound detection systems such as hydrophones and hydrophone arrays. The sensor operates at its resonant frequency as a single-axis, in-plane, capacitive sensing accelerometer with two mechanically coupled sensing elements, and it possesses inherently dipole directionality. The mechanisms for sound detection using this sensor are discussed, and an engineering approach to underwater sound detection in a neutrally buoyant configuration is demonstrated. The sensitivity of the sensor was 0.81 V/mg (-131.9 dB re 1V/μPa), and its noise spectral density was 95 μV/√Hz. Cross-axial sensitivity was -13 dB. Measurements verified that the sensor's characteristics operating in air did not change while operating underwater in a neutrally buoyant configuration.

THIS PAGE INTENTIONALLY LEFT BLANK

TABLE OF CONTENTS

LIST OF FIGURES

THIS PAGE INTENTIONALLY LEFT BLANK

LIST OF TABLES

THIS PAGE INTENTIONALLY LEFT BLANK

LIST OF ACRONYMS AND ABBREVIATIONS

CAD	computer aided design
DNR	dynamic range
MEMS	Micro Electrical Mechanical System
MFLI	multi-function lock-in
NB	neutrally buoyant
NPS	Naval Postgraduate School
NSD	noise spectral density
PCB	printed circuit board
PVC	polyvinyl chloride
SNR	signal-to-noise ratio
SRL	Sensors Research Lab

THIS PAGE INTENTIONALLY LEFT BLANK

ACKNOWLEDGMENTS

I would like to express my heartfelt gratitude to the Office of Naval Research, Naval Information Warfare Center Pacific, and Department of the Navy for investing in basic research and affording the opportunity for officers to earn advanced technical degrees; Dr. Fabio Alves for his technical expertise, never-ending patience, and friendship; Dr. Gamani Karunasiri for his guidance, wisdom, and even temperament despite every obstacle; Dr. Renato Rabelo for his skill in the laboratory and for his endless teachings; the Naval Postgraduate School Department of Physics for welcoming me into their family and for sharing their technical knowledge with me and the Navy; my colleagues for their support and friendship; and finally, my wife for her forbearance during almost a year of working from home.

THIS PAGE INTENTIONALLY LEFT BLANK

I. INTRODUCTION

A. BACKGROUND

From the first submarine used in combat with the hand-powered *H. L. Hunley* during the American Civil War, to the modern threat of silent submarines, submarine technology has established itself among the most viable of weapon systems. As long as there are weaponized submarines and other undersea vehicles that continue to improve, then advancements in anti-submarine warfare technology, including new sensors, is critical to successful naval operations [1].

Historically, the U.S. has not always been capable of countering undersea threats. At the start of the Cold War, U.S. naval leadership assessed antisubmarine warfare capabilities as lacking, including weapons, doctrine, and sensors [2]. Submarine development and proliferation continues today. The Office of Naval Intelligence projects China will grow its submarine fleet to 76 vessels by 2030 [3]. Although the U.S. Navy as part of 355-ship force-level goal sets to achieve and maintain 78 submarines [4], this may not be enough vessels to counteract the undersea threat from China in addition to the rest of the world.

Just as the undersea threat is well-established, so is the sensor technology. The existing technologies for detecting submarines and other undersea vehicles include sonobuoys [5], which are a system of multiple sensors and hydrophones, which are the underwater equivalent of a microphone. Hydrophones are sensors that often exist as part of large arrays that are towed behind ships [6]-[8]. Most hydrophones are passive devices that transduce the pressure fluctuations from acoustic waves, and sonobuoys combine signals from accelerometers and hydrophones to detect sound.

Despite the maturity of these sensors, the Navy continues to invest in new underwater sensor technology [9]. These investments embody Chief of Naval Operations' priorities including "mastery of the undersea domain" by "driving technical development," and "modernizing our sensors," which is described in the CNO strategic guidance for the future Navy, FRAGO-19 [10].

B. CURRENT PROBLEMS WITH UNDERWATER DETECTORS

Localizing undersea threats is challenging with the current technology. Since traditional hydrophones may exhibit limited directionality and there is ambiguity in the relative bearing to the sound. As a result, localizing undersea threats can be problematic. For passive underwater acoustic detectors, vector sensors have been a good alternative "since they are sensitive to both magnitude and the direction of the acoustic wave" [6]; however, more than one sensor is typically required, as is the case with sonobuoys. Processing data from multiple sensors is computationally heavy and may require complex algorithms [11]-[12].

Another problem with hydrophones is their size and weight. Current towed array hydrophones have a diameter of several inches and require a large shipboard space for a powerful handling and stowage system [13]. Reducing the size and weight of any particular shipboard equipment increases the hull's stability, weight margin, and may provide flexibility for key weapons system additions [14]. Additionally, the total weight of equipment on a ship, or payload, is an especially important factor in the capability of smaller vessels. There is a non-linear relationship between a ship's size and its total payload—as the ship size decreases, the payload "can often decrease more quickly, making the smaller ship not just less capable than the larger ship, but proportionately less capable" [15]. In order to maintain capability in smaller ships, innovative equipment solutions are necessary.

C. STATUS OF RESEARCH

Since these limitations of hydrophones are well known, much underwater acoustic detector research focuses on improving the directionality characteristics of hydrophones and designing small form-factor sensors. New technology presented in research generally involves combining sensors into small arrays and algorithmically determining sound pressure level and direction of sound arrival [16], or designing inherently directional sensors, such as Micro Electrical Mechanical System (MEMS) (accelerometers) or other vector sensors [6].

Previous underwater sound detection research at the Naval Postgraduate School (NPS) Sensor Research Laboratory (SRL) explored inherently directional, *Ormia ochracea* (*Ormia*)-based MEMS sensors. To support the Navy's needs for technological development,

studies are investigating if *Ormia*-based sensors can be an effective alternative for more complex or bulky systems. Experimentation on this sensor began with goal of detecting and localizing acoustic sources in air; however, the NPS *Ormia*-based sensor was recently adapted for underwater operation. Previous research concludes that because of the *Ormia*-based sensor's small size (<4 mm), low-power consumption, and promising performance, it has the potential as a next-generation underwater sensor [17].

A unique aspect of the *Ormia*-based sensor is that from a single sensor, directional information can be retrieved, which reduces data collection, signal processing and computational efforts. Minimizing the load on data transportation and computational systems is imperative as "it is anticipated that the … amount of data produced by unmanned systems will continue to exponentially increase" [18].

Two MEMS sensor configurations have been studied at the SRL. One configuration included submerging the *Ormia*-based sensors in silicone oil and housing them in a flexible, sound-transparent enclosure. This configuration proved to work well underwater [17]. In addition, researchers investigated a near-neutrally buoyant configuration, where the *Ormia*-based sensor was housed in an air-filled, hermetically sealed enclosure which allowed the sensor to operate as a directional accelerometer. Building on the latter, ***the objective of the thesis is to determine if Ormia-based MEMS sensors can be used in a neutrally buoyant (NB) configuration to measure the particle acceleration as well as the direction of arrival of sound.***

To accomplish this objective, the following research questions must be answered: Will the *Ormia*-based sensors maintain the same characteristics in a NB configuration as in air? Is it possible to test directionality of a neutrally buoyant configuration using NPS facilities? What are the characteristics of a NB sensor assembly and how do they compare with other sensor technology that is looking to detect and localize underwater sound?

In order to answer these questions, a review on NB designs and previous research was performed, a NB enclosure was designed and fabricated following previous research best practices, and the sensors and enclosure were thoroughly characterized in air and underwater.

D. THESIS ORGANIZATION

Research focused on improving current underwater, *Ormia*-based sensor technology, as well as building on the understanding of the sensor's localization and sensitivity performance. Chapter II provides a literature review, highlighting sensor configurations, performance, as well as advantages and disadvantages. Chapter III outlines the basic principles of the *Ormia*-based sensor and provides details on a neutral-buoyant sound detection scheme. Chapter IV presents experimental results summarizing the *Ormia*-based sensor's capabilities as an underwater sensor in a neutrally buoyant configuration. Experiments included characterization of the sensor's frequency sensitivity and directional responses both in air and underwater as well as noise spectral density measurements. Chapter V summarizes the observations and experimental results and offers further insight into the sensor's overall performance as well as recommendations for future work.

E. BENEFITS OF THIS STUDY

Although hydrophones and sensor array technologies are still serving as reliable tools, they still have limitations, as previously emphasized. Current systems are physically large or require computationally intensive signal processing, require multi-sensor arrays, or may even require the ship to maneuver in order to detect and localize sound. A small sized-sensor would take up less space and tonnage on a ship. Additionally, smaller sensors have the potential to be carried by unmanned vehicles as either a permanent system on larger vehicles, or as part of a "leave behind" surveillance sensor [19]. Similarly, a small, lightweight sensor could even be used as part of a towed array on glider [20]. Finally, it is possible that more sensors could be carried in the limited space onboard anti-submarine warfare capable aircraft. If smaller, directional sensors are deployed, a single helicopter would be able to carry more sensors and interrogate a greater area [21].

By studying a new, compact sensor that can detect the magnitude and direction of sound, there is a potential for developing an affordable, highly scalable Advanced Undersea Warfare System [22] that works toward achieving strategic future Navy goals.

II. CURRENT RESEARCH OF ACOUSTIC PARTICLE VELOCITY AND ACCELERATION DETECTORS

This chapter outlines some of the research into directional underwater acoustic sensors. A well-established method of detecting sound is measurement of the medium's particle velocity under oscillatory motion from an acoustic pressure wave (pressure gradient-sensors) [23]-[25]. This sensed pressure is then proportional to the sound pressure level. Hydrophones are the primary sensor used for detecting acoustic waves, but they have bearing ambiguity. Most sound detection schemes rely on two or more sensors to determine the direction from which sound is originating. The information from each sensor in the array is then processed via a time difference of arrival or finite difference measurement technique. Even still, there can be ambiguity between which side of the sensor array the sound originated. The following paragraphs present previously researched techniques that sought to overcome these challenges.

In 1956, Leslie et al. were among the first to document efforts to measure the particle velocity of water using a neutrally buoyant hydrophone. Their theoretical and experimental results concluded that a velocity pickup mounted in a neutrally buoyant, rigid, spherical shell is capable of measuring particle velocity. The theoretical analysis determined that the sensor and enclosure need not be neutrally buoyant, although a negative buoyancy decreases sensitivity, and positive buoyancy increases sensitivity. Additionally, their research presented sensitivity measurements that were consistent with changes in static pressure and temperature, and the response was flat from 15–700 Hz with a sensitivity of 0.18 V/(cm/s). They also concluded that the directional response of the velocity sensor is better at low frequencies than high frequencies, proving over -20 dB of cross-axial sensitivity. The researchers attributed this to a lack of the hollow brass sphere's mechanical rigidity at higher frequencies resulting in "appreciable transverse response" [26]. With their promising results, the authors laid the groundwork for further research on neutrally buoyant directional sensors.

Ten years later, Bauer and DiMattia continued research on directional underwater sound sensors using "moving-coil transducers under mass control that impedance matches

the fluid medium" [23]. Bauer and DiMattia claimed the hydrophone exhibited "high sensitivity and precise polar patterns" [23]. This research on a mass controlled, moving-coil transducer was also studied by others later.

Similar to both Leslie and Bauer's research, in 1985 Gabrielson et al. sought to measure the acoustic particle velocity of the surrounding water with a neutrally buoyant, "glass-microballoon-and-epoxy composite" cylinder [27]. Their underwater enclosure encased a commercially available geophone, which worked on the identical principle as Leslie's [26]. Compared to Leslie's work, Gabrielson's efforts were designed to reduce distortion of the acoustic field in an easier-to-build underwater enclosure. As a result, their sensor presented a strong agreement in source level measurements when compared to the reference hydrophones. The authors note that a single sensor used to measure the particle velocity can be beneficial in cases where the pressure gradient must be measured, but insufficient separation between two hydrophones is impractical [27].

A different approach in designing a sensor with intrinsic directivity is a polyvinylidene fluoride (PVF2) biomorph, as studied by Josserand and Maerfeld in 1985. Their researched showed that a flexible PVF2 biomorph's piezoelectric properties allowed for a dipole directional response at 60 Hz with a 25 dB signal level difference between sound incident at 0º and 90º. The bimorph's sensitivity was -190 dB re 1V/μPa from 1 to 4 kHz, although it was not completely flat [28]. The significance of this research is that it presented a new type of hydrophone that measures direction and absolute sound intensity with a single sensor.

Another approach for an underwater, MEMS, direction-finding inertial sensor as studied by Rockstad et al., in 1996, was an "electron-tunneling transduction mechanism" [29]. The micromachined sensor was made up of a hinged, cantilevered proof mass with a tunneling tip. To sense proof mass vibrations on its cantilever, the edge of the proof mass contains an electrode that interacts with a second cantilever tunneling electrode. Their research goal was to develop and test a miniature directional sensor "with a self-noise below 100 nano-g/√Hz from 5 to 1000 Hz" [29]. The two orthogonally packaged sensors were to be housed in a neutrally buoyant spherical shell. Shaker table laboratory testing of

a single-axis electron tunneling sensor showed “a noise floor from 1 micro-g to 10 nano-g/√Hz” [29], which the authors noted was an order of magnitude lower than similarly sized traditional cantilever accelerometers. Although the authors expressed plans to test a two-axis “neutrally buoyant directional hydrophone,” they did not publish any further articles [29]. Since the ambient ocean noise floor is quiet, this research is significant in that the authors documented a unique development in designing a low-noise underwater, directional sensor.

Similarly, Moffett et al., at the Naval Undersea Warfare Center, Newport studied a “piezoelectric, flexural-disk accelerometer” in a neutrally buoyant configuration [30]. In their 1998 paper, they presented the detailed design parameters and experiments of two lead zirconate-titanate disks with a resonant frequency of 11 kHz. The accelerometer sensitivity was -22 dB re 1 V/g with a “spectral noise-equivalent acceleration floor” of -51 dB re 1 g per √Hz, and the pressure sensitivity was approximately -240 dB re 1V/Pa [30]. Since Moffett et al.’s research exploits similar detection schemes to those explored in this thesis, their results offer a good source of comparison.

In 2004, Kim et al. published yet another common technique utilizing a pressure-acceleration, or “p-a intensity probe” [31]. They proposed system of sensors, or “vector sensor,” that included a near-neutral buoyant piezoceramic cylinder which houses two accelerometers. The cylinder detects the acoustic pressure while the accelerometers detect the acoustic particle acceleration. The authors note that their findings are important in that their vector sensor is compact and thus can be used for “near field intensity mapping,” and it also has the capability to extract the “active, propagating intensity of a source from a reactive field due to reverberation,” which would be not be possible with an omnidirectional hydrophone [31]. Kim et al., in 2008, continued studying this p-a sensor and proved its ability to determine directionality and sound energy in a complex, near-field acoustic field containing two sound sources of different sizes at different distances from the sensor. Such a conclusion is important for real-world sound radiation mapping to “reveal localized regions of sound production” [32].

Recently, Hari and Chandrika presented a unique development with particle velocity measurements with a sensor that “utilizes nature-inspired bionic hair-based transduction” [33]. The authors note that hair-based acoustic vector sensors generally suffer from low sensitivity. Instead, they focus on simulations of a cantilever, transducer-mounted fiber laser interferometer that takes advantage of a horn-style particle velocity amplifier. Their simulations found that the horn velocity amplifier, depending on fluid dynamic viscosity, resulted in between 90% attenuation and 3.6 times gain. [33]. Perhaps the horn-style amplifier technology could be exploited for stationary sensors, it is impractical as mobile, deployable sensor.

In 2017, Bahreyni et al. presented a “wideband, low-noise accelerometer intended to replace existing hydrophones in towed arrays” [34].The researchers designed a silicon-on-insulator MEMS sensor displaying a sensitivity of 4.0V/g, a low noise spectral density (NSD) of 350 ng/√Hz, and a dynamic range of 135 dB. Not only did the micromachined accelerometer present an ability to measure the sound intensity, but it also exhibited a directional response with a cross-axial sensitivity of 30 dB. The resonant frequency of the tested sensor was 4.4 kHz and had a sensitivity of approximately -197 dB re 1V/μPa [34]. Their results offer improvements in sensitivity and noise from Moffett’s results two decades earlier.

In 2018, Choi et al. researched the possibility of determining acoustic direction of arrival through an array of sensors (two hydrophones and an inertial measurement unit) by making a “probabilistic estimation of time delay that was formulated and calculated using a Bayesian update process” [35].Although their research offered a relatively reliable method to determine the incident angle of sound, their method required multiple sensors and complex signal processing algorithms.

Also in 2018, Roh et al. studied a “shear type accelerometer,” used in conjunction with hydrophones to use for localization and characterization of acoustic sources [36]. Their efforts focused on the detailed structural design of the accelerometer to optimize the vector sensor system. The researched accelerometer produced a dipole response with a cross-axial sensitivity of -20 dBV, and when the accelerometer was paired with an

omnidirectional hydrophone, a cardioid polar response was produced. Their accelerometer also proved to have a receiving voltage sensitivity of -204.9 dB (re 1V/μPa). Comparing to Bahreyni, Roh's sensor showed similar performance.

Researchers in China presented a unique bio-inspired MEMS vector sensor in 2009, outlining a "four-beam-cilia" based off of fish lateral line system [37]. Although their structure's directional response did not accurately determine the direction of sound arrival, the sensor concept is interesting.

Also in China, Zhang et al. in 2014 studied an Integrated Circuit Piezoelectric accelerometer encapsulated in a polyurethane, possibly neutrally buoyant cylinder, that was designed to "move freely along with the sound wave." The researchers claimed a sensitivity of -185 dB re 1V/μPa at 100 Hz, and unstable results beyond 1000 Hz (due to "high sensitivity" of the sensor). The accelerometer measured 20 mm by 20 mm and required a large, co-vibration, elastic mounting system measuring 1.7 inches by 5 inches. The sensitivity measured on a shaker table was approximately 7.8 V/g [38].

Another Chinese approach taken by Lieu et al. in 2016 was measuring the particle acceleration of sound by employing an "acoustic dyadic sensor" made of an array of two accelerometers mounted in a large, acoustically transparent, neutrally buoyant sphere [39]. The sensitivity of the sensors was not reported, and the directivity diagrams showed asymmetric responses. The authors indicate the influence of fabrication on directivity, as well as numerous "theoretical and engineering design problems" [39].

Despite the many efforts to develop a simple, easy to manufacture, and small-sized vector sensor with good performance characteristics, there has been limited openly published success. Armed with the knowledge from previous research, we conducted experiments on an *Ormia*-based sensor to detect and localize sound.

THIS PAGE INTENTIONALLY LEFT BLANK

III. MEMS NEUTRALLY BUOYANT INERTIAL SENSOR DESIGN AND CONSTRUCTION

1. Introduction

A unique type of specially designed acoustic sensor is presented in this thesis in the form of a biomimetic MEMS-based device. By mimicking the unique, mechanical structure of the *Ormia Ochracea* parasitoid fly's hearing system, a MEMS sensor can detect both the magnitude and direction of incident sound [40]. A scanning electron micrograph of such a sensor used in this thesis is shown in Figure 1. The micrograph shows the sensor construction of two wings (1) which are connected via a bridge (2). The wings and bridge are then connected to the substrate (4) by two torsional legs (3). Under sound excitation, the wings vibrate into and out of the "plane of the page." These vibrations are transduced to an electrical signal via comb-finger capacitors (5) that are attached at the ends of the wings [41]. Two identically designed sensors of the same family are presented in this research, 6–1-2 and 6–1-3, where "6-1" represents the sensor family, and "2" or "3" represents the sensor serial number.

Previous Naval Postgraduate School (NPS) research for sound detection exploited this phenomenon using *Ormia*-based MEMS sensors as pressure gradient detectors [41]-[45]. In these studies, the wings of the sensors were directly exposed to acoustic pressure waves, either in air or sealed underwater in an enclosure filled with a dielectric oil. In each case, the acoustic wave would propagate through the medium and the pressure from the oscillating fluid particles would impart a force on the sensor's wings allowing for sound detection.

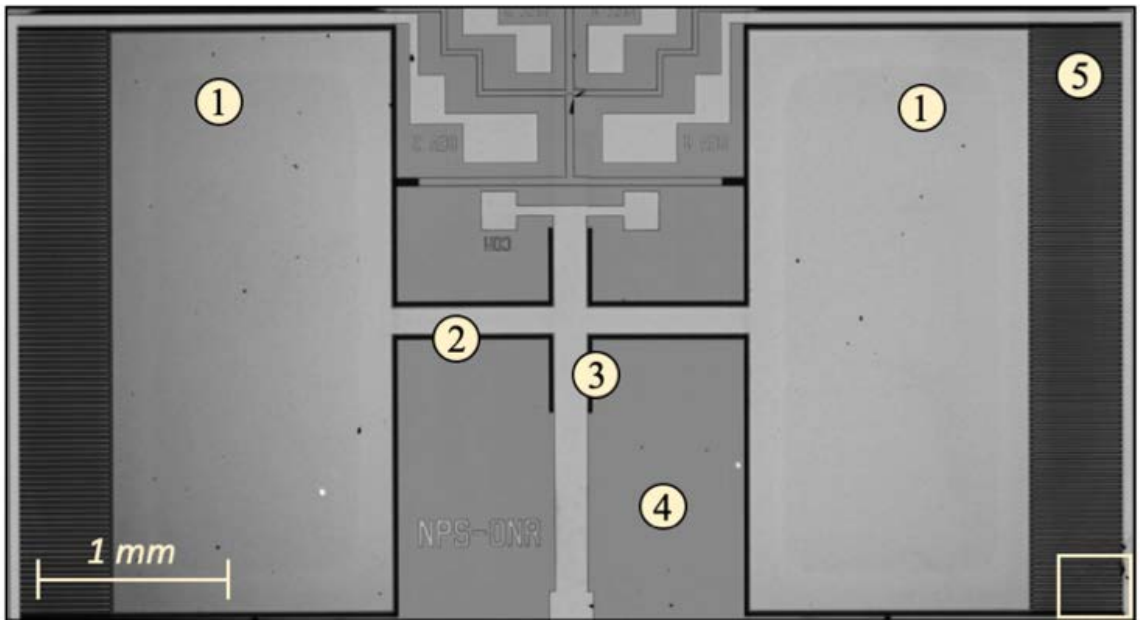

(1) Wings. (2) Bridge (mechanically couples both wings). (3) Torsional leg (couples the bridge, and thus the wings, to the substrate). (4) Substrate (where the structure is anchored). (5) Interdigitated comb finger capacitors (provide differential capacitance for electronic readout).

Figure 1. Scanning Electron Microscope micrograph of the MEMS

Not only can the *Ormia*-based sensor be used in direct contact with a sound wave in fluid, but it can also be used to measure the acceleration of the medium's particles as they oscillate back and forth with an acoustic pressure wave. Since the *Ormia*-based MEMS operate similar to cantilever accelerometers, they are directionally sensitive. The *Ormia*-based MEMS sensor (here on referred to as "the sensor") can operate as an underwater inertial sensor when packaged within a neutrally buoyant shell, or "enclosure" (the shell's mass is equal to the mass of the displaced fluid).

As a sinusoidal longitudinal wave passes through a medium, particles will oscillate about its equilibrium position, which is between t_1 and t_2 in Figure 2. Under the influence of a wave, a particle, shown in red, will accelerate from its position at t_1 to its position at t_2. It will continue to oscillate back and forth in a sinusoidal motion with the acoustic wave.

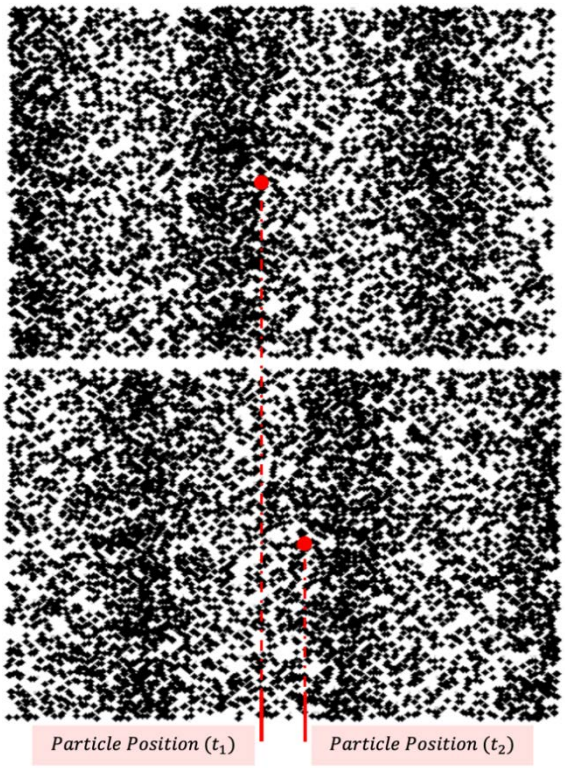

A single particle is shown in red. As the wave propagates, the particle oscillates sinusoidally about its equilibrium position.

Figure 2. Particle oscillation in a longitudinal wave. Adapted from [46].

The particle motion velocity-potential is “interpreted physically as impulsive pressure,” and that “immersed solids may be free to take the motion imposed upon them by the fluid pressures” [47].As such, a neutrally buoyant enclosure in an underwater acoustic field will undergo an oscillatory motion as a result of the fluid pressure, and its motion will be “identical to the motion of the water particles” if the enclosure was removed [26]. Alternatively stated, “if the sensor body is neutrally buoyant, then the sensor body acceleration is equal to the fluid particle acceleration” [31].

2. Design of the NB enclosure

To operate underwater, the sensor must be mounted inside a watertight enclosure. If this enclosure is neutrally buoyant, then it will undergo acoustically stimulated oscillations, and the sensor will transduce these oscillations. One important aspect to achieve this transduction is the sensor (Figure 1) must be rigidly mounted to its underwater

enclosure. In this configuration, as the enclosure oscillates with the acoustic wave, the sensor's wings (acting as proof masses) deflect via the torsional legs from the inertial force imparted by the moving substrate. As a result, the distance between the moving comb fingers at the wings' tip and the fixed combs changes. Total capacitance increases as the combs are closer to each other, and decreases as they move apart, and this capacitance is electronically read out [48]. Further details on this sensor's operation are well-documented in [40]-[41] [49]-[50].

As shown in Figure 3, the sensor is mounted on an in-house developed printed circuit board (PCB) that contains a charge amplifier based electronic readout. The PCB is rigidly mounted with bolts to a 3D printed housing. Also placed on the PCB is a Meggitt Model 22 piezoelectric type accelerometer (here on referred to as "the accelerometer") which operates in the shear mode, and is positioned to operate along the same axis as the sensor [51]. The accelerometer is positioned on the PCB approximately 5 mm beneath the sensor using the manufacturer's petrol-based mounting wax. Though typically mounted rigidly, accelerometers can be mounted using manufacturer-supplied petrol wax with assumed minimal sensitivity deviation. Specifically, due to the accelerometer's small size (3.76 mm diameter casing) and light weight (0.14 grams), the mounting wax is assumed to only attenuate the response at higher frequencies outside of the frequency bandwidth of interest [52]. The Meggitt 22 accelerometer was chosen because of its low mass, which limits its interference from mass-loading effects [51]. A detailed view of the 3D printed housing is shown in Figure 4. The sensor's PCB slides into the slot and is secured in place with nylon bolts. A cavity underneath supplies space for cabling.

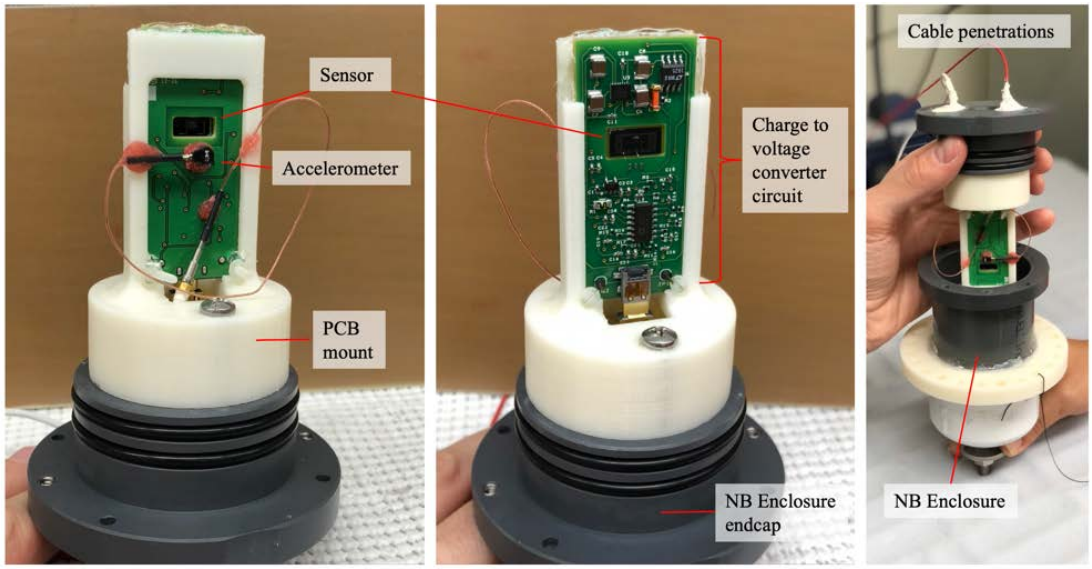

All photos show an assembly of the sensor mounted on the PCB rigidly held in a 3D printed mount, which is in turn rigidly bolted to the PVC NB enclosure end cap with a double O-ring seal. Left: Rear of the PCB showing the accelerometer mounted with petrol wax. Middle: Front side of the PCB showing the sensor, charge to voltage conversion circuit, and four conductor micro HDMI connector. Right: The assembly loading process.

Figure 3. MEMs sensor in 3D printed mount

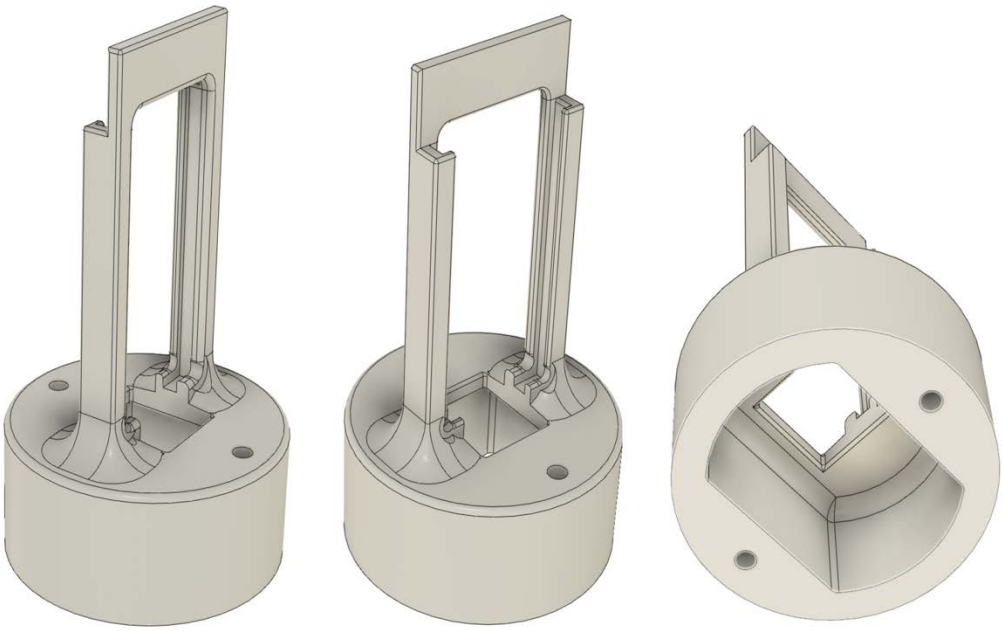

Left: Front side of the 3D printed mount. Middle: Back side of the mount. Right: Underside of the mount. The underside has a cavity to allow for coiling excess signal cables.

Figure 4. 3D printed PCB and sensor mount

The PCB mounted sensor and the accelerometer are encapsulated in a watertight enclosure NB enclosure. The PCB is bolted to the 3D printed mount, which is bolted to a removable PVC plug with a double O-ring seal. This plug seals into one end of a 2-inch PVC pipe that is sealed off permanently on the other end with a cemented hemispherical PVC pipe fitting. PVC was chosen for simplicity of construction. Due to the tight double O-ring seal, a vent plug is provided on the lower endcap to maintain atmospheric pressure in the enclosure during assembly. A 3D printed stabilizing ring provides for an anchoring point stabilizing string, described later. The assembly scheme is outlined in Figure 5.

Top row, left to right: PCB and sensor (white cutout); PCB in 3D printed mount; 3D printed mount attached to NB enclosure removable end cap with vent plug. Bottom row, left to right: Removable cap in cylindrical tube (gray); permanently cemented endcap (white); enclosure with stabilizing ring.

Figure 5. NB enclosure design and construction

The enclosure is ballasted to be nearly neutrally buoyant. Important design characteristics of this watertight enclosure include (a) ability to finely adjust the buoyancy, (b) symmetrical shape so the sensor's directional response is easily interpreted and is undistorted by the enclosure orientation. Additionally, the suspension system should stabilize the enclosure underwater and should (a) not interfere with vibrational response of the enclosure, (b) maintain a desired sensor orientation, and (c) allow for the enclosure, and thus the sensor to move in response to the acoustic wave [31].

The enclosure is stabilized with thin, multi-filament string suspending the enclosure from a support bar. The support bar is attached to a rotatable rod extending to the water's surface. A CAD representation of this setup is presented in Figure 6. The stabilizing strings are attached to a 3D printed support ring and constrain the rotation of the NB enclosure so that the sensing plane and directional response is not influenced by enclosure rotation.

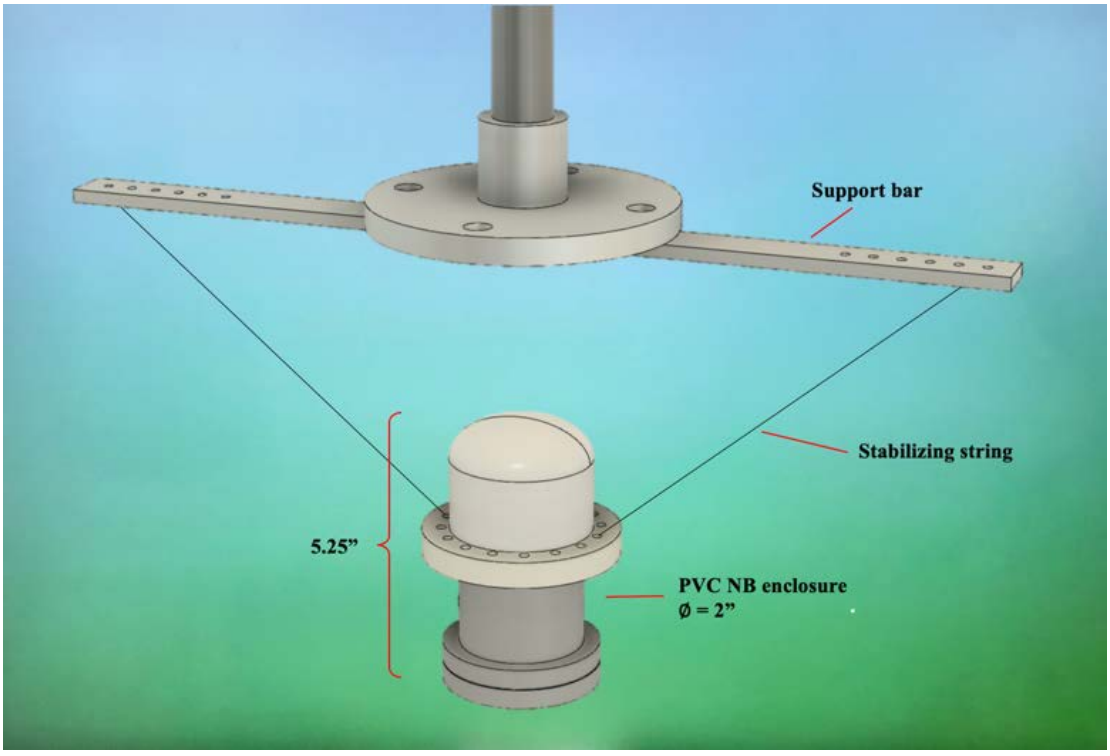

Figure 6. CAD representation of NB enclosure underwater

Ballasting of the enclosure is achieved by a bolt that is glued to the upper PVC end cap. Fine adjustments are made to the ballast by adding or removing mass, in the form of nuts and washers, to the bolt. The sensor's signal and power were fed through the enclosure with a four conductor, 32AWG shielded wire that was loosely coiled beneath enclosure to minimize affecting enclosure motion. The ballasting scheme is shown in Figure 7. For mass and volume characteristics of the enclosure see Appendix G.

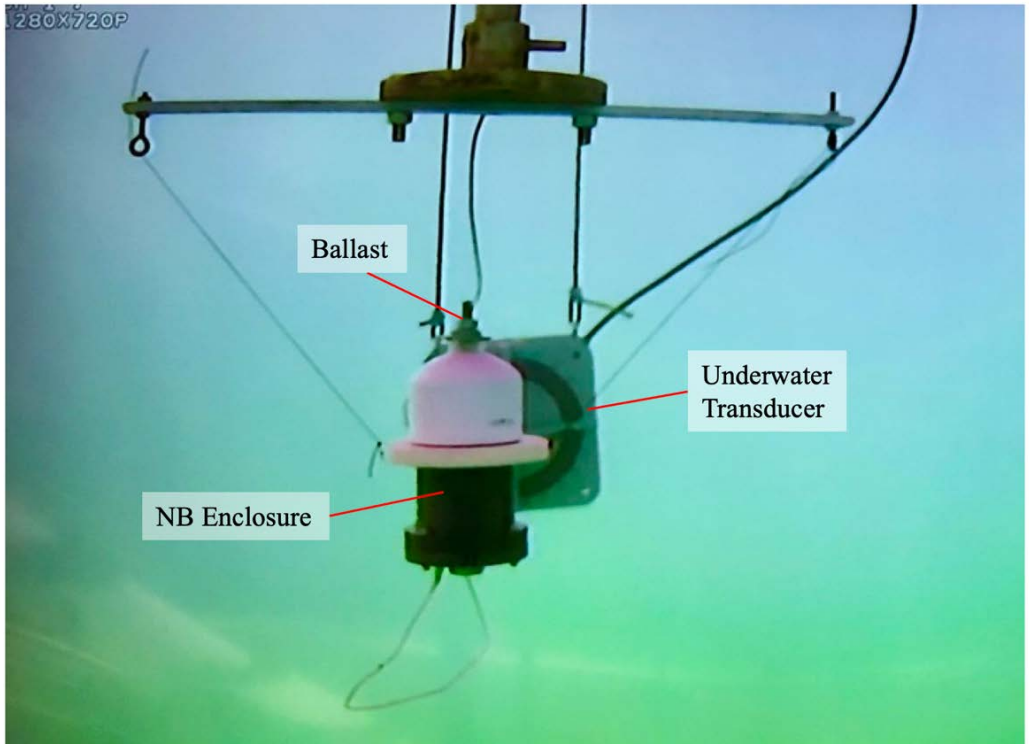

Figure 7. Ballasted NB enclosure underwater with transducer

IV. EXPERIMENTAL RESULTS

This chapter describes experiments carried out to characterize the sensor's performance, both in its spectral sensitivity and its directionality. To understand the sensor's inherent characteristics, experiments were first conducted in air without the NB enclosure. In order to quantify the effect of the enclosure on the sensor's response, experiments were then conducted in air but with the sensor encapsulated within the NB enclosure. Finally, in order to answer the main research questions, characterization of the sensor's performance was carried out underwater. This chapter presents a comparison between in-air and underwater responses, as well as offers a comparison to other neutrally buoyant underwater sensors.

A. SENSOR CHARACTERIZATION IN AIR

First, the sensor was tested in air in the anechoic chamber without its PVC NB enclosure. In this configuration, the sensor acts as a pressure gradient microphone [53]. The functional diagram showing the basic equipment set up for this characterization in the anechoic chamber is shown in Figure 8. Signal conditioners for the reference microphone and for the accelerometer are not shown.

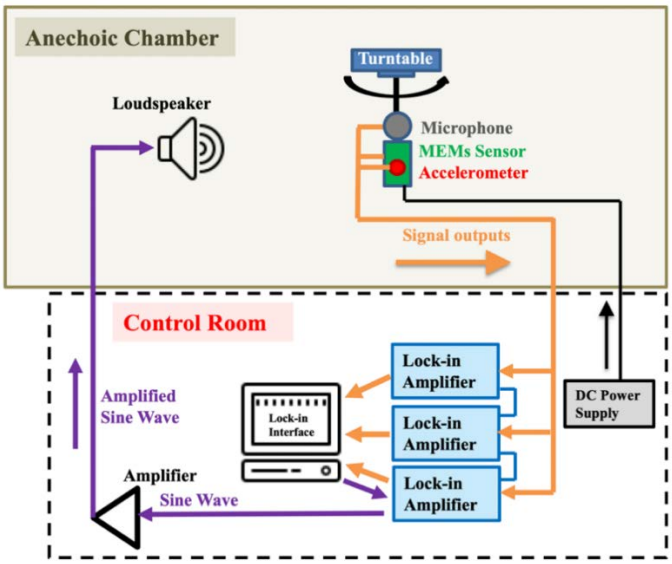

Figure 8. In-air sensor characterization functional diagram

Figure 9 shows the experimental setup with the sensor, accelerometer, reference microphone, and speaker in the anechoic chamber. Both the sensor and the accelerometer are pictured on the PCB, and the microphone is above the PCB at the same distance from the speaker. Reference pressure for signal normalization is provided by the calibrated microphone's response. +/- 5 VDC from an Agilent DC Power supply model E3620A powered the sensor. The sensor's signal output from the charge-to-voltage converter circuit was read by a Zurich Instruments Multi-Function Lock in Amplifier (MFLI). An Endevco Signal Conditioner Model 2775A converted the accelerometer's charge to voltage, and also passed the accelerometer voltage to a second MFLI. Finally, a PCB Piezotronics Model 482C Signal Conditioner with a gain of 100 fed the microphone's response to a third MFLI. Zurich Instruments LabOne software controlled and synchronized all three MFLIs, which permitted simultaneous measurements of the sensor, the accelerometer, and the microphone. The master MFLI also served as the sine wave signal generator. A Techron power amplifier Model 5507 amplified this sine wave and passed it to a JBL 2380A Bi-radial horn inside of the anechoic chamber. The horn was positioned 2 meters away and its height and direction were aligned directly on axis to the sensor, microphone, and accelerometer.

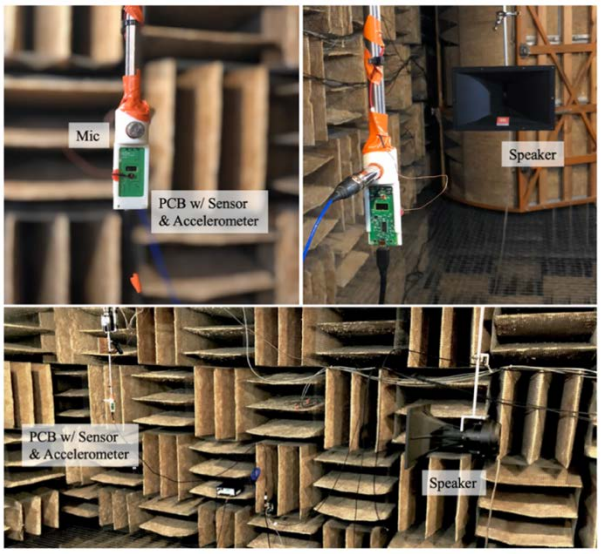

Top left: Front view of the sensor and microphone. Top right: Rear view of the sensor and microphone facing the speaker. Bottom: Wide angle view of both the sensor and the speaker

Figure 9. In-air sensor characterization experimental setup

1. Frequency Response

In order to measure the frequency response of the sensor, microphone, and accelerometer, the LabOne software swept through 200–2000 Hz to excite the JBL horn. To prevent saturating the sensor output at resonance, the MFLI and the power amplifier settings were adjusted. It was found that that pressure at the sensor needed to be less than 6 mPa at 1 kHz for preventing saturation. Figure 10 shows the sensor's frequency sensitivity (V/Pa), and the peak at 692 Hz corresponds to its mechanical bending mode. The sensitivity was obtained by dividing the voltage output of the sensor by the applied sound pressure as recorded by the calibrated reference microphone (see Appendix A). The frequency response's shape is typical for sensors of this kind [44].

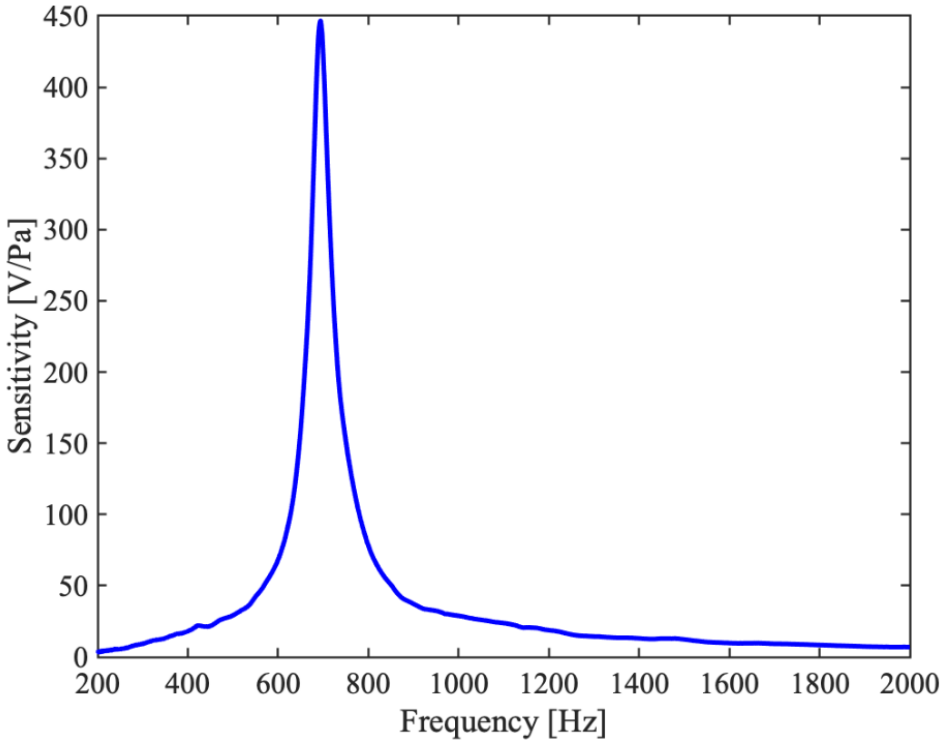

Figure 10. In-air frequency response (6-1-2 sensor)

Figure 11 shows the acceleration of the PCB normalized to the applied sound pressure. Using the approach described in Appendix B., the accelerometer's voltage output

was converted to acceleration in milli-g's. Due to the low sound level from the speaker for frequencies lower than 500 Hz, the PCB acceleration was not measurable and the accelerometer's output was only noise. Above 500 Hz, however, the speaker provided sufficient sound pressure to consider the data in Figure 11 as valid. The sound excitation resulted in approximately 50 mg/pascal of PCB acceleration at the sensor's resonance of 692 Hz. This acceleration could couple with the response of the sensor. PCB vibrational modes are further explored in Section 3(b) of this chapter.

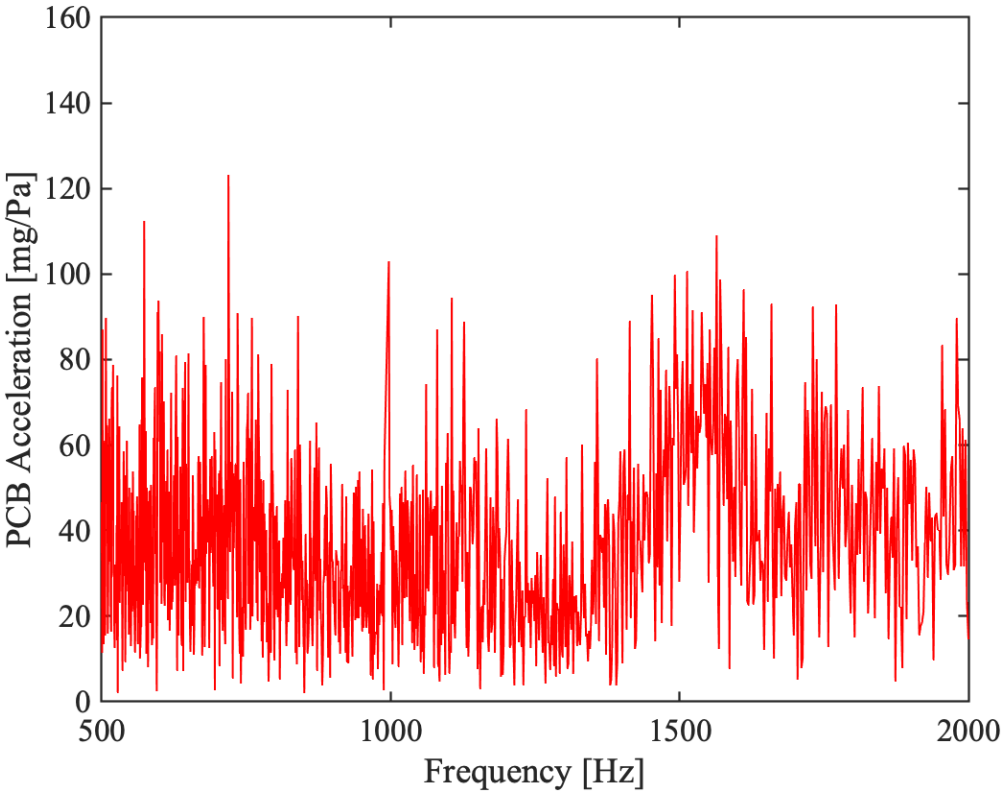

Figure 11. In-air frequency response (PCB mounted accelerometer)

2. Directional Response

The JBL speaker was excited at a fixed level and frequency (692 Hz) while the turntable rotated the sensor and the accelerometer at constant speed of 1 degree per second. Figure 12 shows the sensor and accelerometer's resulting directional response. The sensor's directional output is typical for sensors of this nature [44], with a dipole response

and over -30 dBV cross-axial sensitivity. The slight asymmetry between the response at +90º and -90º is likely due to either small asymmetries in the hand-applied, UV adhesive mounting of the sensor to the PCB, or from slight offsets in the mounting angles on the turntable. Since the accelerometer's output is very close its noise floor, there is no observable correlation between incident angle and accelerometer output. A small ripple is observed in the sensor signal output, and this ripple is likely due to mechanical coupling between the sensor and the motor of the turntable via the pole connecting the sensor board to the rotator (See Appendix D). When the turntable motor is off, there is no observable ripple.

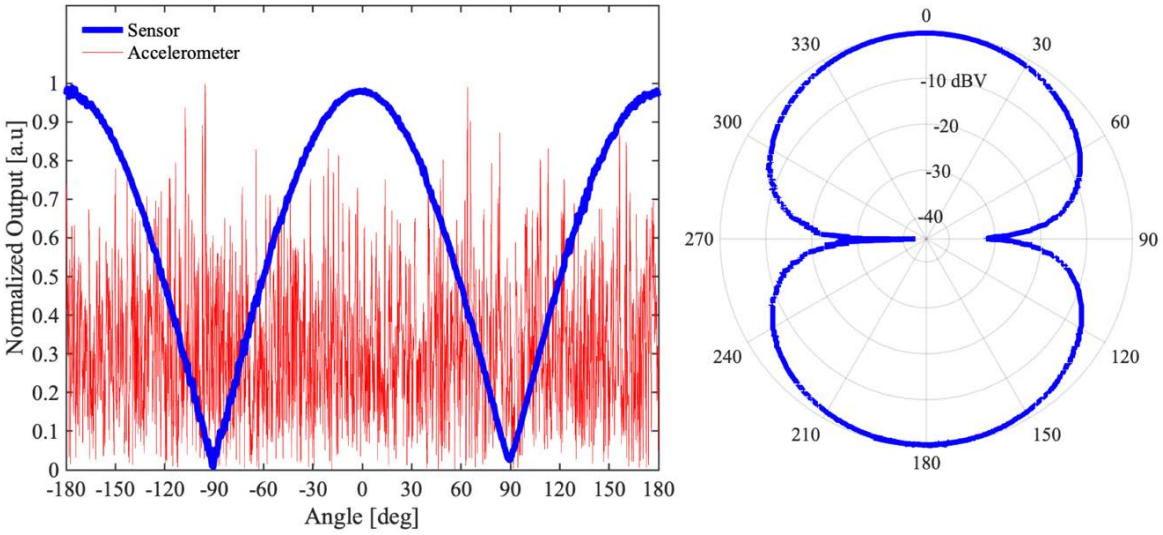

Left: Sensor and accelerometer's directional measurements in which both devices outputs were normalized by their maximum output. Right: The same data displayed in a polar plot in units of dBV, and the maximum device voltage was normalized to 0 dBV.

Figure 12. In-air directional response at 692 Hz (6-1-2 sensor and accelerometer)

3. In-air Linearity Test

In addition to a frequency sweep, the linearity of the sensor's response was tested. The JBL speaker was driven at the sensor's resonant frequency of 692 Hz, and the sound pressure was lowered in steps by decreasing the power amplifier's output voltage. Figure

13 shows that the sensor's output increases linearly with an increase in applied sound pressure, as observed earlier for such *Ormia*-based sensors [41].

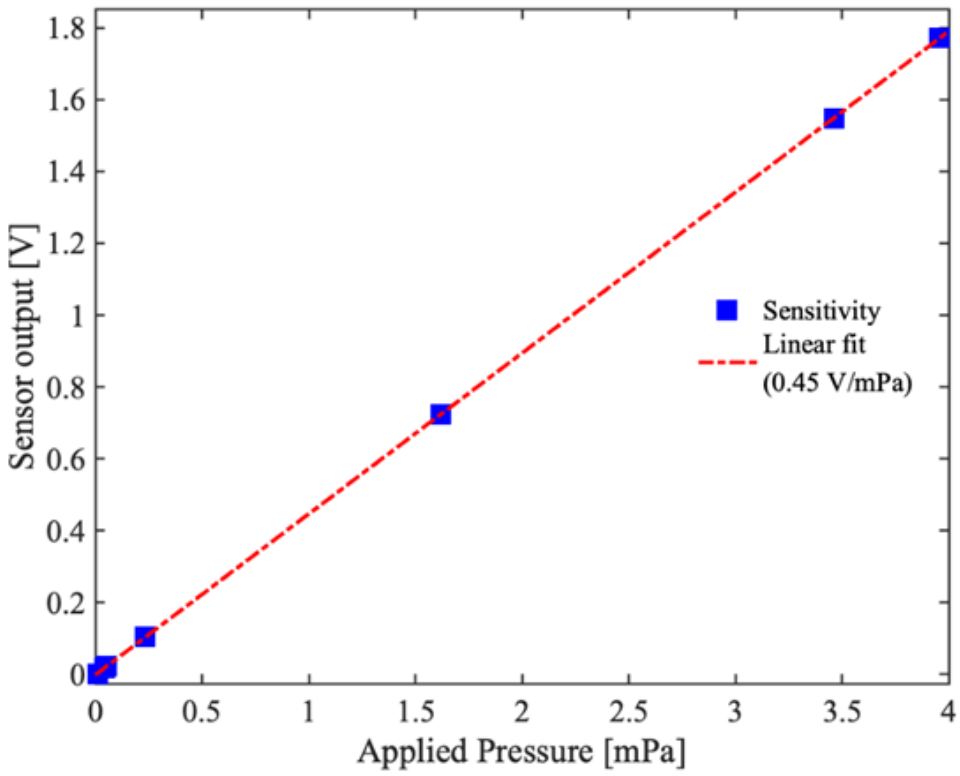

Figure 13. In-air linearity test (6-1-2 sensor)

The PCB acceleration was simultaneously recorded by the accelerometer as the sound pressure was varied, but the acceleration was constant near zero. There were no observable steps coinciding with the changes in applied sound pressure.

B. SENSOR CHARACTERIZATION WITH THE NB ENCLOSURE

To test the sensor's operation as an accelerometer, the sensor was placed in its hermetically sealed NB enclosure as in Figure 3 (right photo) and Figure 5 (bottom right photo), and measurements were conducted in the anechoic chamber.

1. Frequency Response

To measure the frequency sensitivity of the sensor in its enclosure, an experiment was set up as illustrated Figure 14 and Figure 15. The speaker's power amp was adjusted to achieve approximately 1 pascal of sound pressure at 1 kHz as recorded by the calibrated reference microphone. The NB enclosure's support bar was perpendicular to the direction of the acoustic wave propagation (top left of Figure 15) and the speaker was excited by the MFLI from 200–2000 Hz, and the outputs of the sensor, accelerometer, and reference microphone were once again recorded.

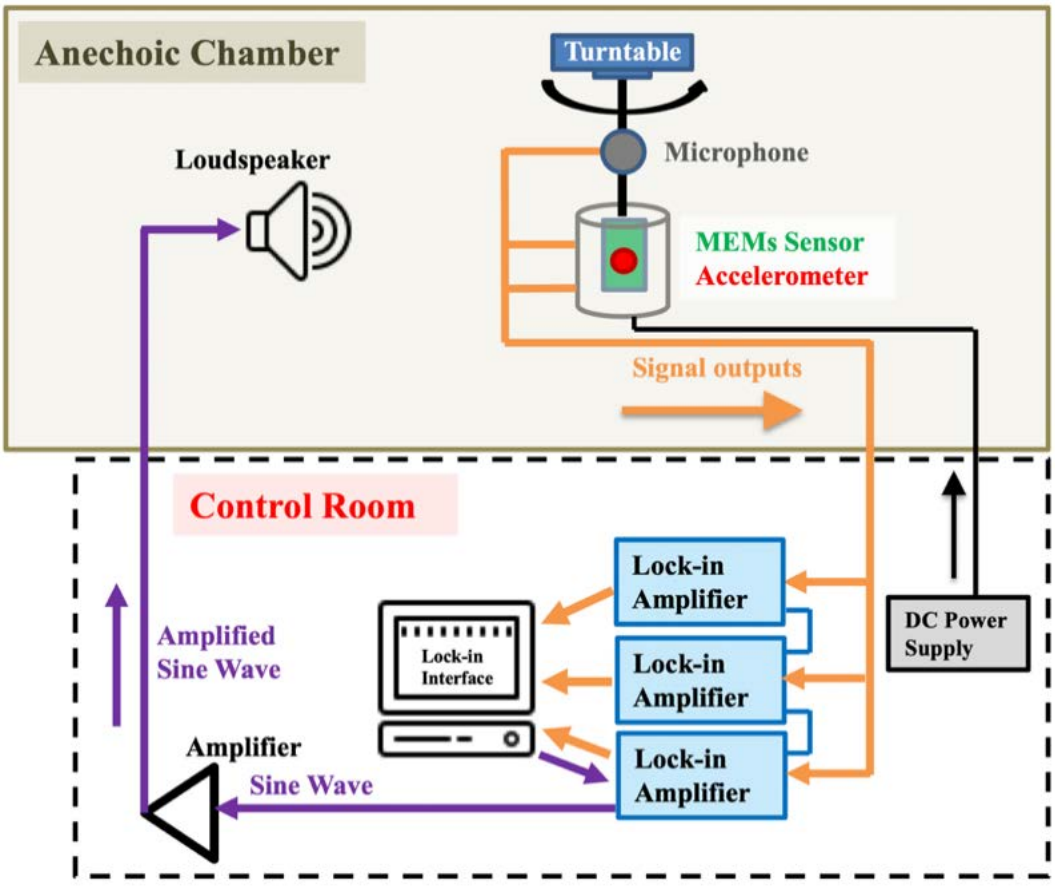

Figure 14. In-air sensor characterization with NB enclosure functional diagram

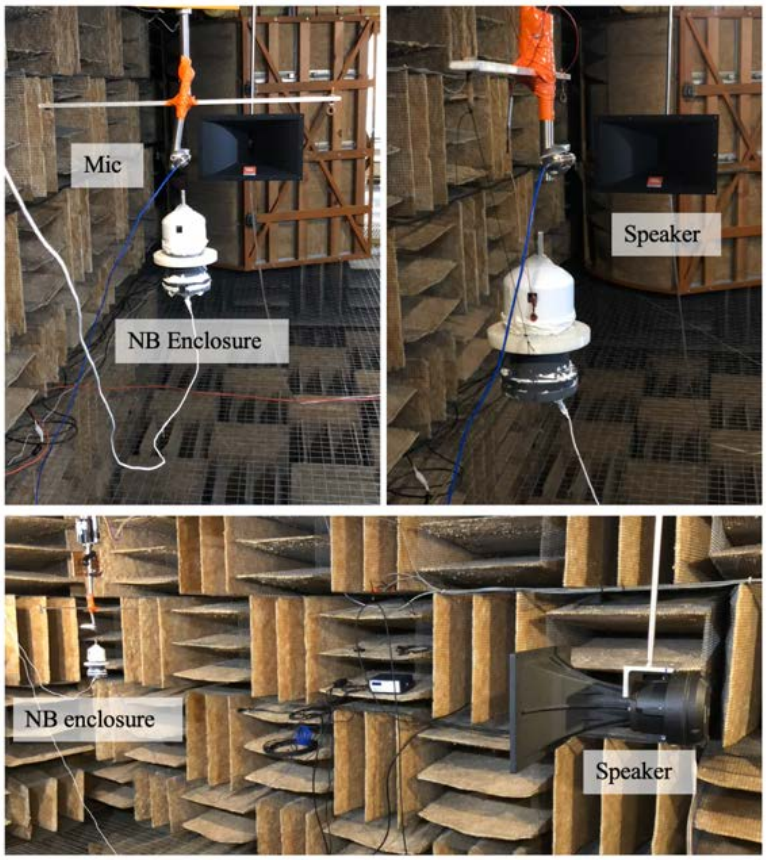

Top left: Support bar mounted perpendicular to the direction of acoustic wave propagation.
Top right: Support bar mounted in line with the direction of acoustic wave propagation.
Bottom: Wide angle view of the experimental setup.

Figure 15. In-air sensor characterization with NB enclosure experimental setup

Figure 16 shows the results of the sensor frequency response experiment. In contrast with the sensor without the housing, which only had one resonant peak at the sensor's resonant frequency, the response presented several distinct peaks in this test, including peaks at 255 Hz, 1050 Hz, 1440 Hz, 1920 Hz, in addition to its resonant frequency of 692 Hz. The origin of these extra peaks, which will be further explored later, are due to both structural resonances of the enclosure, and the PCB on which the sensor is mounted. Sensitivity of the sensor at 692 Hz was 1.26 V/Pa, which is two orders of magnitude less than its sensitivity measured without the enclosure. The decrease in sensitivity is expected since the sensor in this case was only measuring the oscillation of the enclosure rather than directly measuring the acoustic pressure wave.

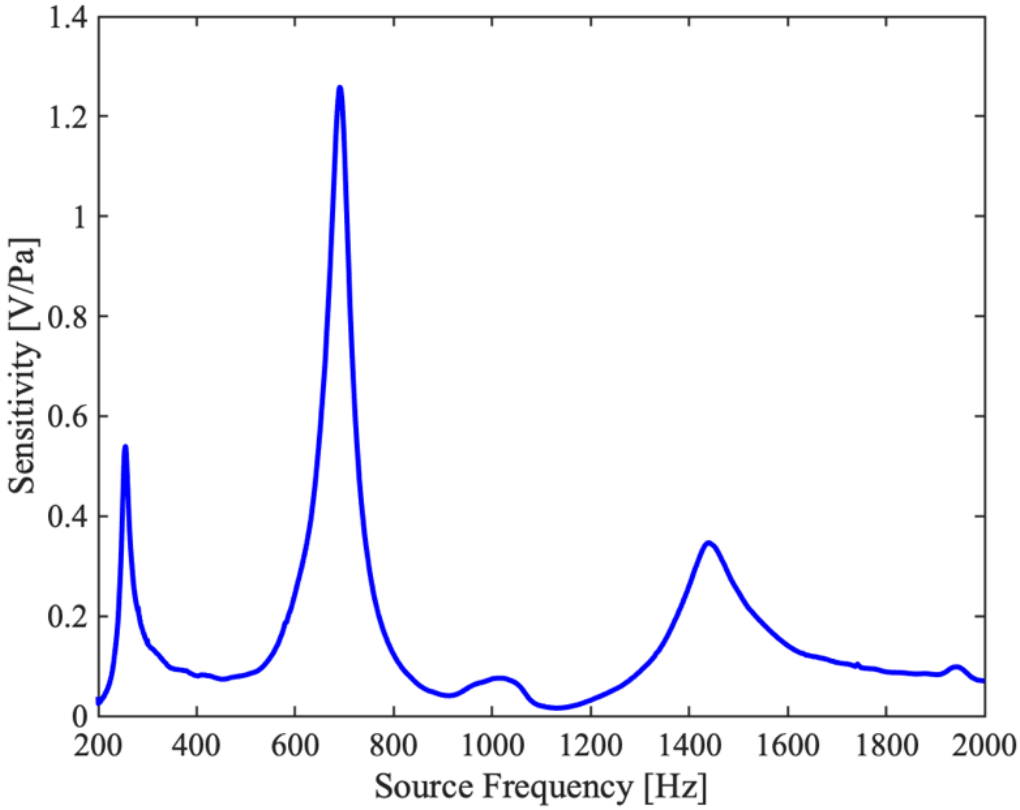

Figure 16. In-air frequency sensitivity with NB enclosure (6-1-2 sensor)

The accelerometer's response was also recorded and is shown in Figure 17. Common with the sensor's response, peaks presented at 255 Hz, 1440 Hz and at 1920 Hz. The accelerometer's null at 1075 Hz is not consistent with the calibration curve of the accelerometer, nor does the null correlate with a null in the sensor's response at the same frequency. Additionally, this null does not coincide with a null of the sound source. As such, it may be a limitation of the accelerometer or the signal conditioner. More experiments are required to verify the source of this null. Note that the reason the accelerometer does not show a peak at 692 Hz like the sensor is because the PCB where the accelerometer is mounted is not resonating at this frequency.

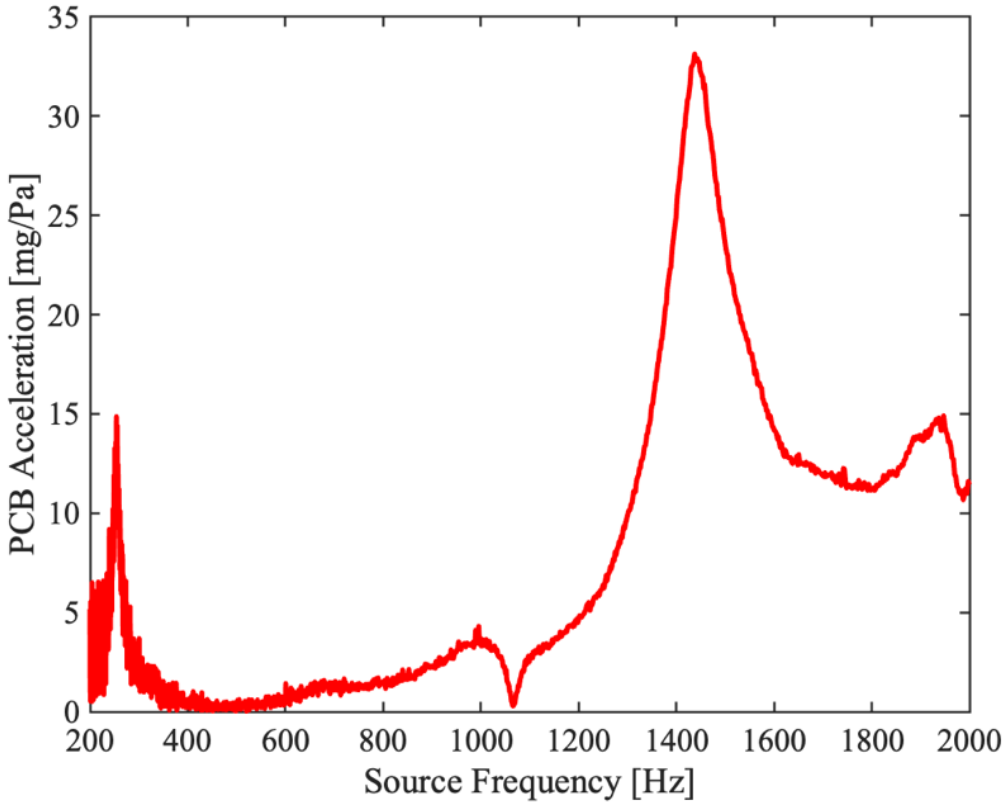

Figure 17. In-air PCB acceleration with NB enclosure (accelerometer)

To better understand the sensor's inertial sensing capabilities, the acceleration of the PCB was used to normalize the sensor's response, as shown in Figure 18. This figure shows the sensor's inertial sensitivity in units of Volts/milli-g, and the curve was obtained by dividing he results of Figure 16 by those in Figure 17. The sensor's resonant sensitivity was 1.2 V/mg and its sensitivity was relatively flat at 10 V/g above 1200 Hz, as indicated. The peak at 1075 Hz is a result of the null at the same frequency in the accelerometer's response.

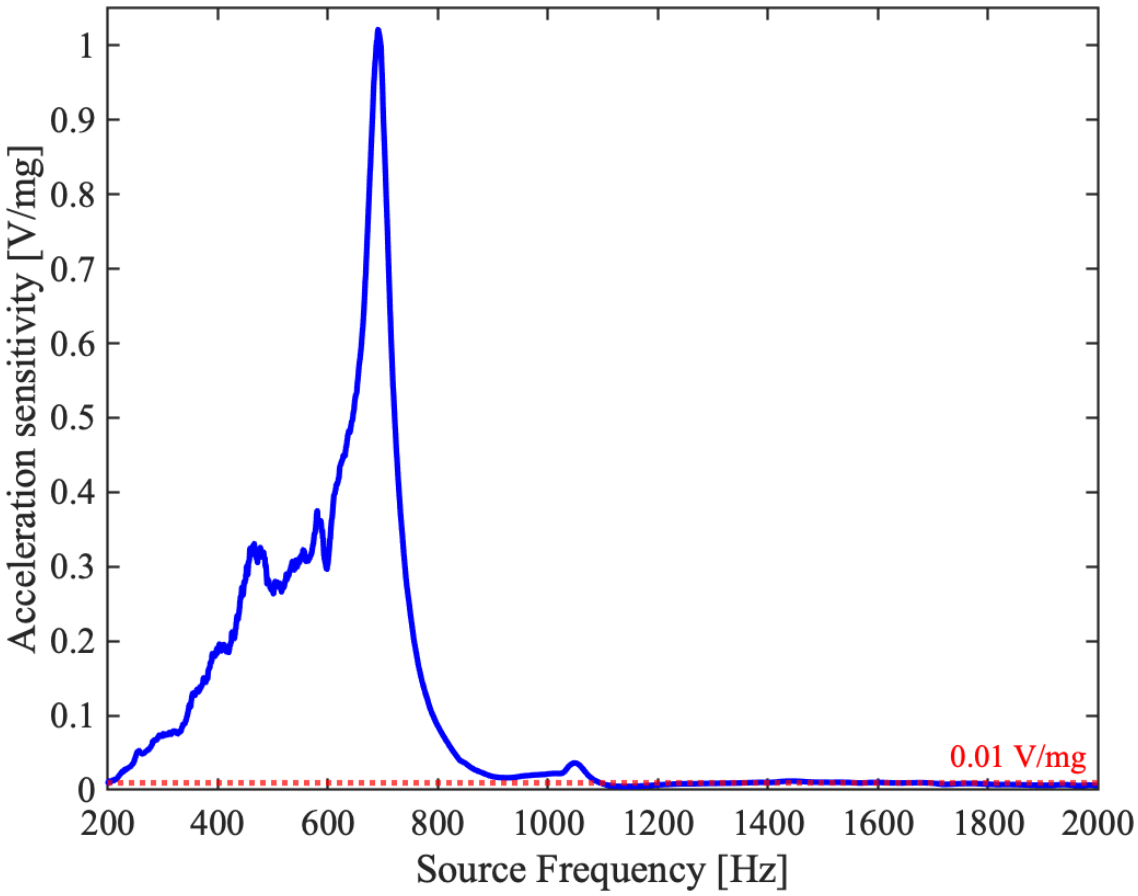

Figure 18. In-air acceleration sensitivity with NB enclosure (6-1-2 sensor)

2. Directional Response

The directional response of the sensor in its NB enclosure was tested at the sensor's resonance of 692 Hz with the same experimental setup. In this test, the sound pressure was held constant at 1 Pascal and the turntable was rotated at 1 degree per second for one full revolution. Simultaneously, the sensor and accelerometer's outputs were recorded. Their directional responses are shown in Figure 19. The polar plot shows a dipole pattern with approximately -18 dBV difference between the on-axis and off-axis response of the sensor. There is a noticeable angular shift between the sensor and the accelerometer responses, which is most likely due to asymmetries in the hand-mounting of the accelerometer with the petrol-wax. Small offsets in the mounting scheme affect its directional response (see Figure 29 and Figure 30 for directional responses showing less angular shift).

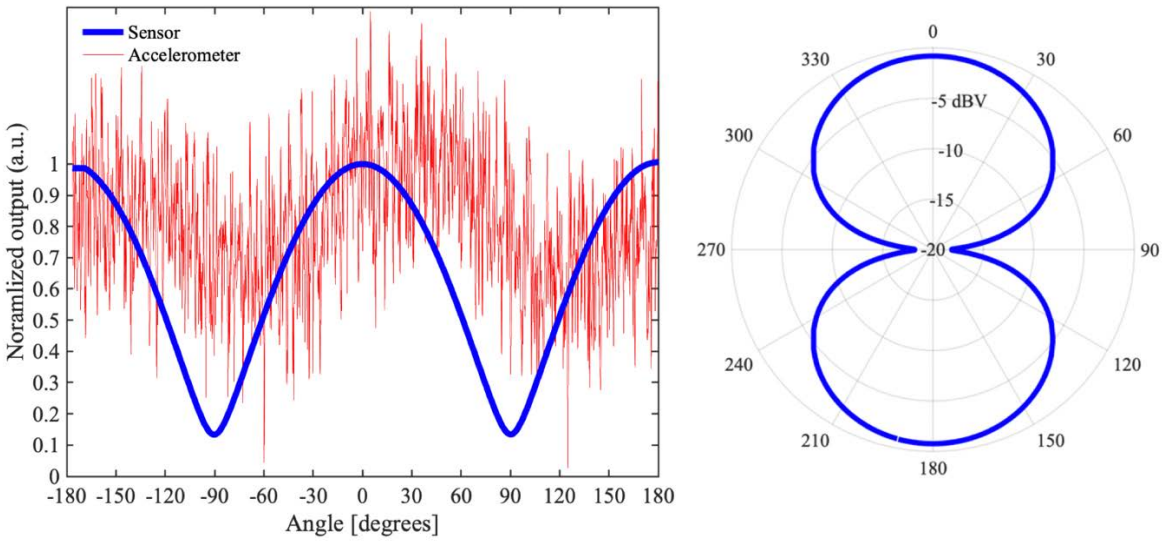

Left: Sensor and accelerometer's directional measurements in which both devices outputs were normalized by their maximum output. Right: The same data displayed in a polar plot in units of dBV, and the maximum device voltage was normalized to 0 dBV.

Figure 19. In-air directional response with NB enclosure at 692 Hz (6-1-2 sensor and accelerometer)

3. Stimulus and Resonant Behavior Study

Since the sensor can operate as both a microphone and as an inertial sensor, it is important to understand what physical stimulus the sensor is responding to. The aim of this thesis is to understand the operation of the sensor as an underwater accelerometer, and as such, it is important to verify that the stimulus is indeed acceleration and not sound transmitted through the housing. Additionally, it is important to understand the influence of the NB enclosure, as well as the sensor's PCB mount on the sensor's frequency response.

a. Sound Transmission through the NB Enclosure

Measurements were again taken in the anechoic chamber to determine the amount of sound transmission through the PVC NB enclosure. Following work in the aircraft industry measuring sound transmission through fuselages [54]-[55], two test conditions were compared: A sound pressure measurement using a the reference microphone directly in contact with the acoustic pressure wave, and a sound pressure measurement using the same microphone within the sealed NB enclosure, as shown in Figure 20.

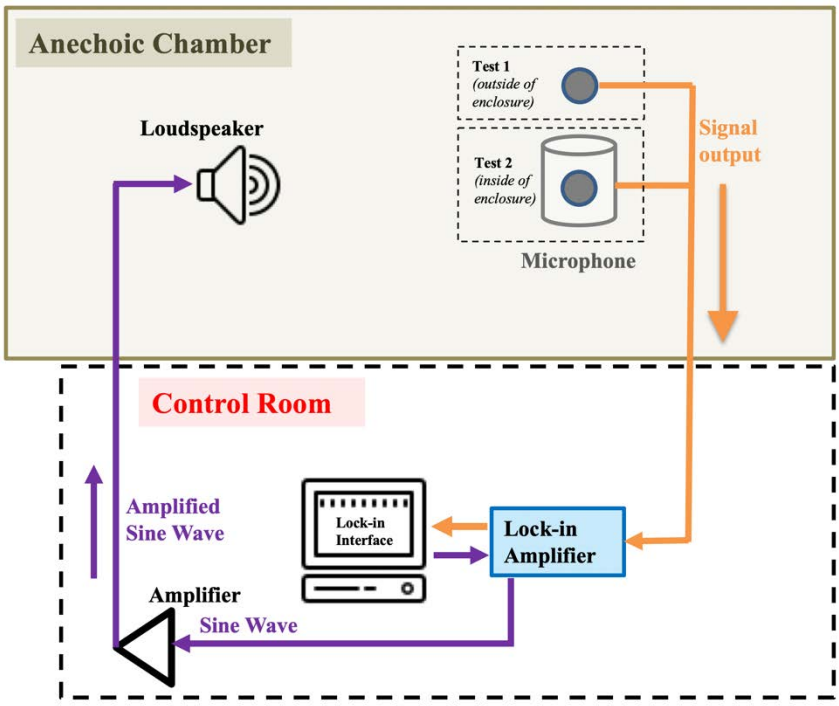

Figure 20. Sound transmission test functional diagram

The center of the microphone's element was positioned at the same height in the cylinder as the MEMS sensor is when it is enclosed. Care was taken to ensure that the microphone was centered close to the axis of the cylinder so that it does not touch the enclosure's walls when sealed in. To eliminate sound transmission into the enclosure through diffraction around the microphone's cable penetration through the end cap, the microphone's cable penetration was sealed using a wad of silicon synthetic earwax. The JBL 2380A Bi-radial horn sound source was positioned directly on axis from the microphone and enclosure, two meters away. This experimental setup is shown in Figure 21.

Left: Exposed microphone. Right: Encapsulated microphone.

Figure 21. Sound transmission test experimental setup

The sound pressure from 200–2000 Hz was recorded inside and outside of the PVC enclosure is displayed in Figure 22. The enclosure was rotated along the long axis of the cylinder and re-secured at different angles of incidence, but the results showed no measurable difference, which is expected due to the symmetric enclosure shape and the omnidirectional response of the microphone. As such, it is assumed that the sound transmission through the shell is likely diffuse, and small angular offsets in the mounting of the microphone within the enclosure have little effect [56]. The pressure that the encapsulated microphone recorded at 692 Hz (the resonance of the 6–1-2 sensor) was 0.175 mPa compared to approximately 1 Pascal measured by the exposed microphone.

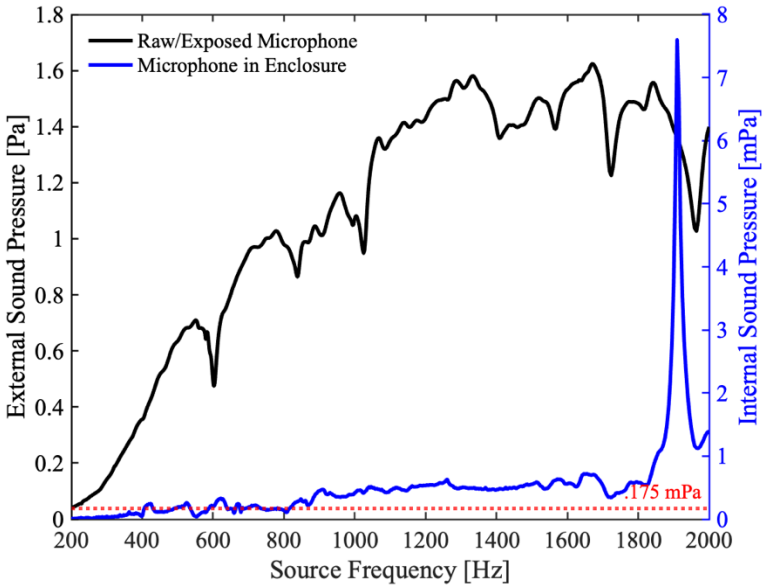

Figure 22. Sound pressure in and outside of NB enclosure

The percentage of the sound wave that is transmitted through the enclosure is calculated by dividing the sound pressure internal to the enclosure (encapsulated microphone) by the sound pressure outside of the enclosure (exposed microphone). This percentage is called the transmission coefficient, and it is shown in Figure 23. It is observable that the enclosure significantly attenuates the incoming sound.

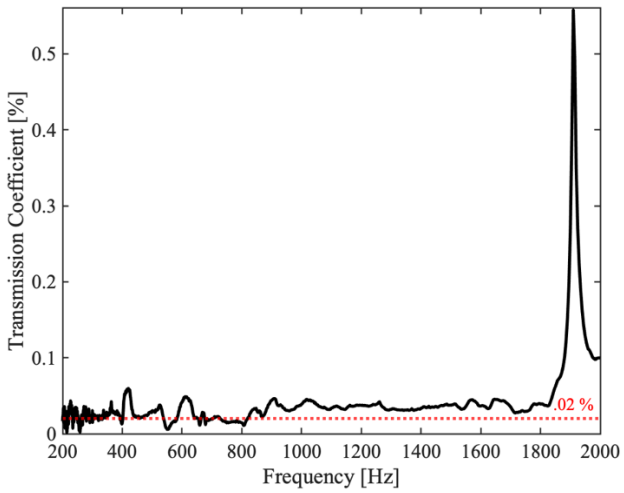

Figure 23. Sound transmission coefficient of NB enclosure

Figure 23 shows that the PVC enclosure provides approximately 0.02% transmission at the 6–1-2 sensor's resonant frequency of 692 Hz. The noticeable decrease in transmission loss around 1900 Hz is likely from the enclosure's structural resonance [57], which is discussed in the next section. The multiplication of the response of the sensor at resonance without enclosure (450 V/Pa) by the obtained transmission coefficient (0.02%) results in 0.09V/Pa. This is the portion of the sensitivity of the sensor inside the enclosure due to sound and not to vibration. Since the total response with enclosure was 1.26 V/Pa, approximately 7% may be due to the transmitted sound.

This experimental procedure provided adequate insight on the transmissivity of the enclosure; however, further investigation may be required to verify the accuracy of obtained results [55] [57].

b. Resonant Characteristics of the NB Enclosure

Aside from transmission of sound through the enclosure, another factor that could influence the sensor's response is vibrational modes of the NB enclosure. Since the in-air response of the sensor in the NB enclosure exhibited extra resonant peaks not characteristic of the sensor's intrinsic frequency response, the origin of these peaks was explored.

To measure the true vibrational response of the enclosure, the NB enclosure was placed in the anechoic chamber for laser vibrometry, as shown in Figure 24. The PolyTec OFV 534 Laser Vibrometer was focused on a small mirror fixed with UV cured adhesive to the upper endcap. The enclosure was excited by sound at a discreet set of frequencies, and the acceleration was normalized to the sound pressure via a calibrated reference microphone. Additionally, as shown in Figure 25, the accelerometer was placed on the outside surface of the enclosure at several different locations, and a discreet frequency sweep from 200–2000 Hz was conducted for each location.

Figure 24. Enclosure vibrational response experimental setup (laser vibrometer)

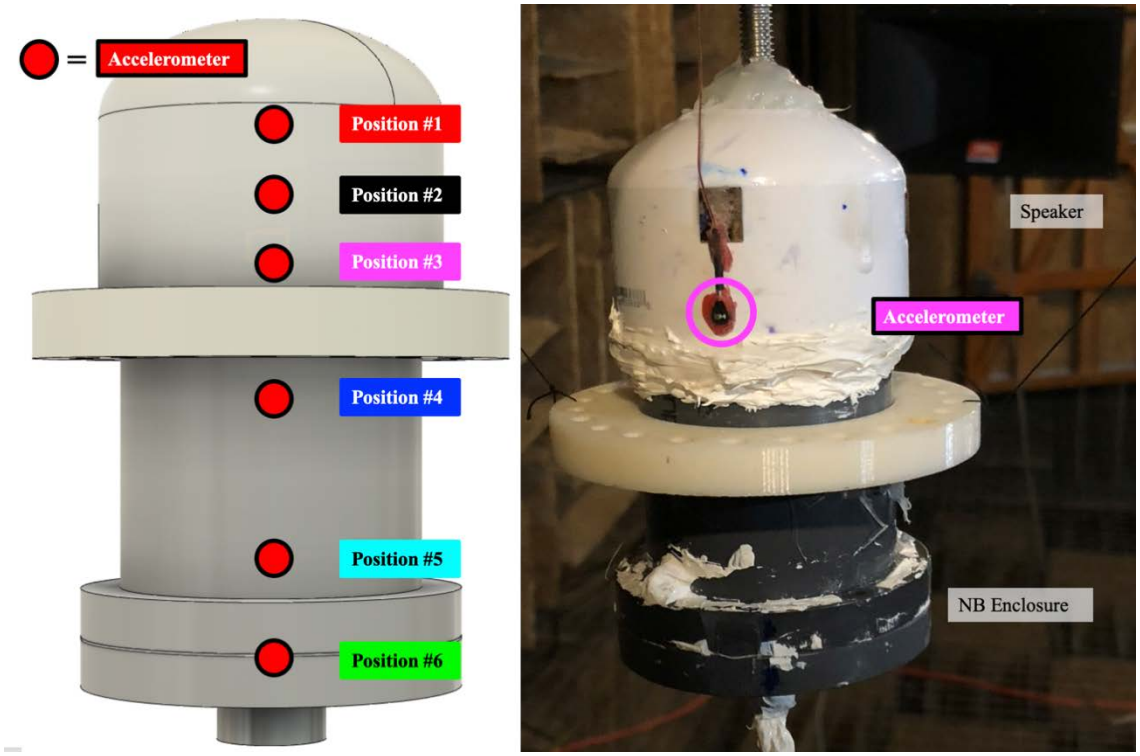

Left: the numbered positions correspond to the location of the accelerometer for each of the vibrational responses presented in Figure 26. Right: depicts the accelerometer in position #3.

Figure 25. Enclosure vibrational response experimental setup (accelerometer)

The measured vibration amplitude using laser vibrometry along with the accelerometer measurements at different locations on the housing surface are plotted in Figure 26. This figure illustrates a few important findings. First, the resonance feature at 1440 Hz observed in Figure 16 and Figure 17 is not observed in Figure 26, therefore this resonance is not due to the enclosure. Second, the enclosure's vibrational response is different at different heights along the enclosure. This may be due to either a torqueing effect on the stabilization ring relative to the center of mass of the enclosure (the lower end cap is more massive and may be dampening out vibrations in this region), or it may be a result the rigidity of the lower end cap (tight fitting O-rings). More experimentation is required to understand the exact mechanism. Third, the peak at 1015 Hz in Figure 16 correlates with an increase in vibration amplitude as measured by the laser vibrometer at the same frequency. Fourth, the relatively strong peak at 1950 Hz, which is explored more later, is most likely due to a structural vibrational mode of the enclosure. As a result, we can conclude that the resonant peaks shown in Figure 17 that can be attributed to the circuit board are 255 Hz, and 1440 Hz, while the peaks at 1040 Hz and 1920 Hz are due to vibrational modes of the enclosure. The peak at sensor resonance (692 Hz) is solely a result of the sensor's bending frequency.

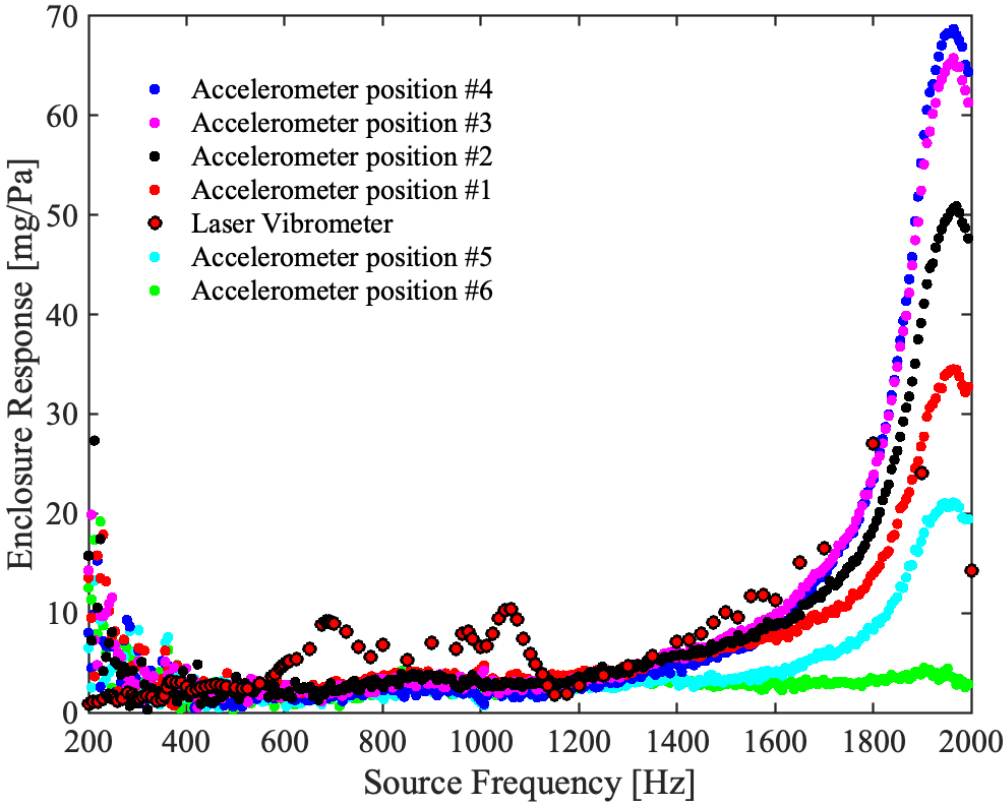

The numbered accelerometer positions correspond with those positions in the illustration in Figure 25.

Figure 26. In-air enclosure vibrational response (accelerometer and laser vibrometer)

The vibrational mode of the enclosure at 1950 Hz was verified by performing a directional response measurement with the accelerometer on the outside of the enclosure and the sensor on the inside. Figure 27, which shows a rotational response of the sensor and accelerometer at 1925 Hz, agrees with the notion of the enclosure is experiencing a structural vibrational mode that can influence the sensor's response. Although the external vibrations are large compared to other frequencies, the sensor's general directional response shape was maintained. It is worth mentioning that the accelerometer data is compatible with a cylindrical cavity inherent oscillatory mode, where a compression in one direction is countered by an expansion on the orthogonal direction. In this case, every 90 degrees the oscillation is aligned with the accelerometer axis, resulting in the maxima shown in red in Figure 27.

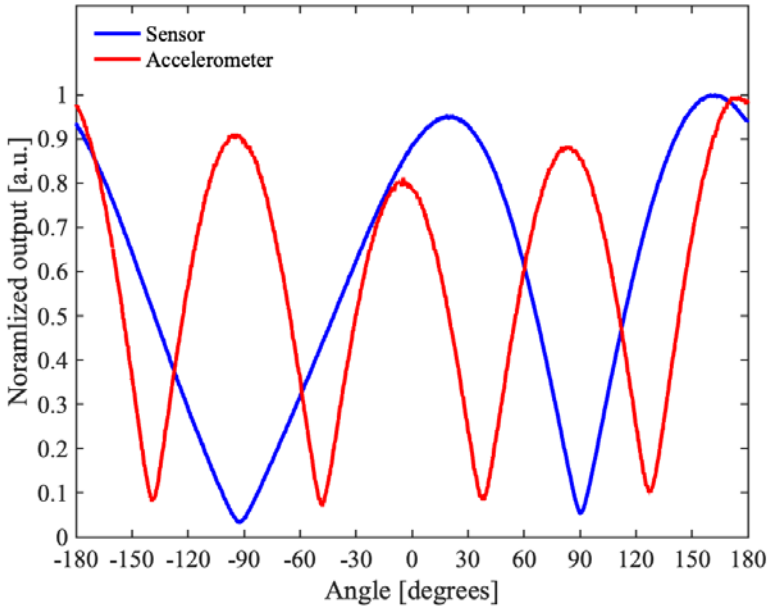

The sensor was located inside of the enclosure in its 3D printed mount, and the accelerometer was located on the outside of the enclosure at the approximate height of the sensor.

Figure 27. Directional response at 1925 Hz (6-1-3 sensor and accelerometer)

Since the enclosure vibration measurements did not reveal any resonant peaks between 1400 and 1500 Hz, yet the sensor showed a resonance in this region (Figure 16), a directional response measurement was performed. A directional response would reveal if either the 3D printed PCB mount or the enclosure itself was inducing additional vibrational modes. With the 6–1-3 sensor mounted in the inside, and the accelerometer mounted on the outside of the enclosure, the speaker was excited at 1490 Hz while the NB enclosure was rotated. Figure 28 shows the resulting directional response of the internal sensor. The sensor maintained its expected directionality, and the accelerometer, which is omitted from the plot for clarity, showed a relatively weak directional response at a structural mode. Since the sensor's response maintained its inherent directionality, it appears that the influence of the structural mode at this frequency is minor. This conclusion is supported by the previously discussed lack of external vibration (Figure 26) at this frequency.

Because external structural modes are not the source of the resonant peak between 1400 and 1500 Hz in Figure 16, it is likely that the PCB and the PCB mount themselves are acting as a cantilever under the influence of the oscillatory motion of the acoustic wave. As the enclosure oscillates with the sound wave, the mount is potentially amplifying this motion like a cantilever. As the enclosure turns towards 90˚, the cantilever no longer moves with the sound wave, which in turn generates the nulls in the response at ±90˚.

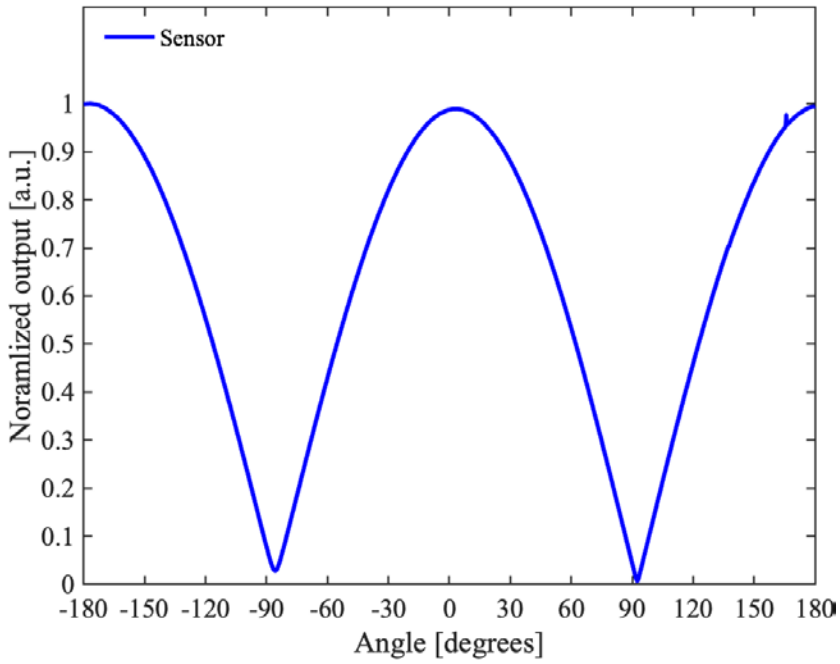

Figure 28. Directional response at 1490 Hz (6-1-3 sensor)

To further verify that the resonant peak of the sensor (675 Hz for sensor 6–1-3) is not influenced by any structural modes of the enclosure or orientation of the support bar, rotational tests were performed with the accelerometer again on the outside and the sensor inside (Figure 29). The test was repeated with the support bar rotated in line (or on-axis) with the direction of acoustic wave propagation (Figure 30). Since both the accelerometer and the sensor show the expected directional dependence, it is reasonable to infer that when excited at 675 Hz, or near the generation 6–1 sensor resonant frequency, there are no additional structural resonant modes influencing the sensor's response and the enclosure is moving in an oscillatory motion with the sound wave.

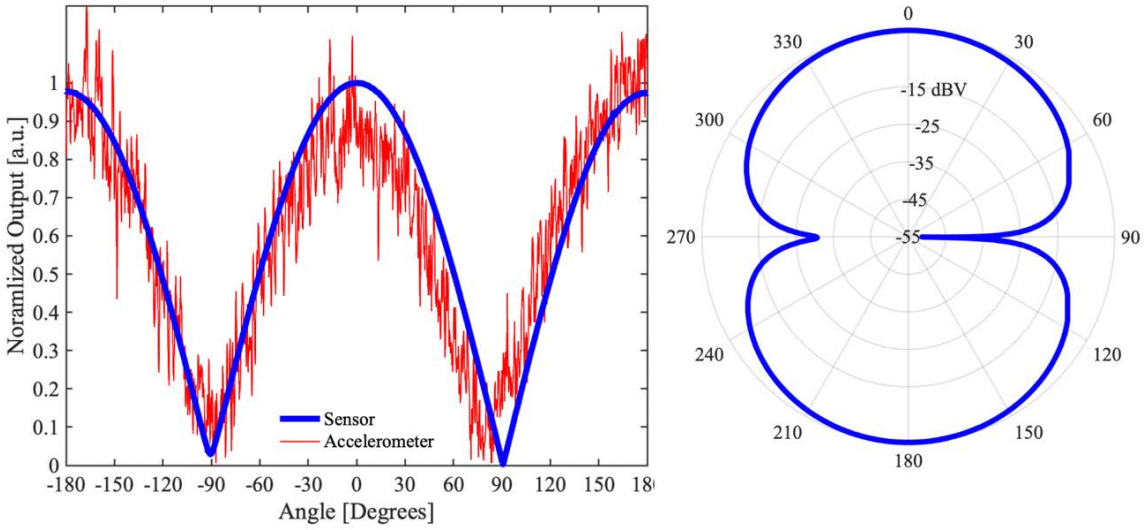

Left: the sensor and accelerometer's directional measurements in which both devices outputs were normalized by their maximum output. Right: the same data displayed in a polar plot in units dBV, and the maximum device voltage was normalized to 0 dBV.

Figure 29. Directional response at 675 Hz (6-1-3 sensor and accelerometer)

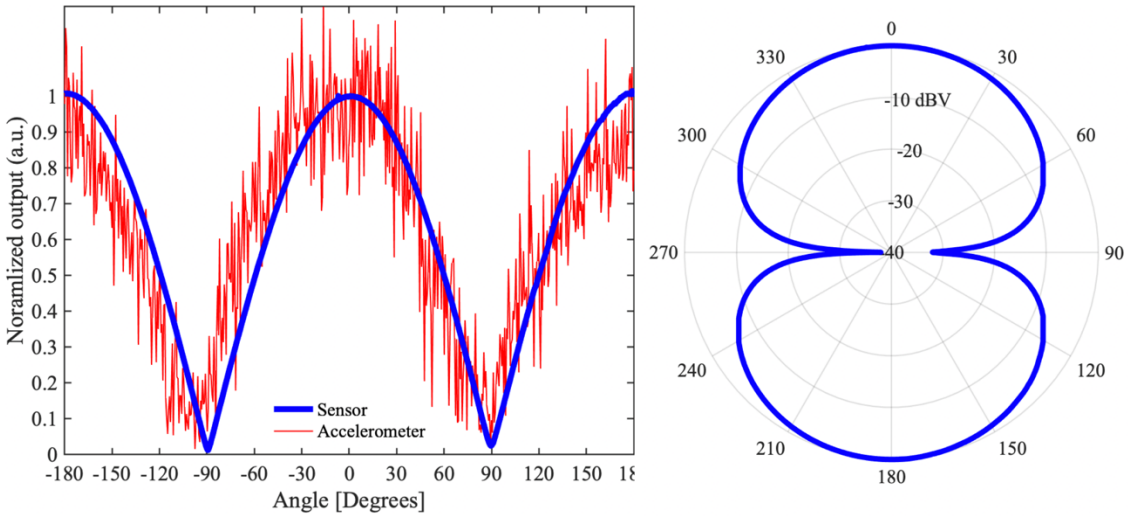

Left: sensor and accelerometer's directional measurements in which both devices outputs were normalized by their maximum output. Right: the same data displayed in a polar plot in units dBV, and the maximum device voltage was normalized to 0 dBV.

Figure 30. Directional response at 675 Hz (on-axis support bar; 6–1-3 sensor and accelerometer)

The slight asymmetry in the both of the directional responses in Figure 29 and Figure 30 is likely due to the asymmetries associated with adhering the sensor to the PCB

or other asymmetries in mounting the PCB, the PCB mount, or the hanging of the enclosure from its support bar. There is a noticeable improvement in cross-axial sensitivity for the 6–1-3 sensor—for the same directional test at sensor resonance, the 6–1-2 sensor showed approximately 18 dBV difference between 0˚ and 90˚ (Figure 19), while the 6–1-3 showed between 30 and 50 dBV (Figure 29 and Figure 30). The root cause of these differences requires further investigation. It may be possible that small structural differences between the sensors and mounting are influencing the cross-axial response.

The effects of the adding mass to the enclosure, as well as changing the orientation of the support bar were also studied and show no significant impact. The results are presented in Appendix F.

C. SENSOR CHARACTERIZATION UNDERWATER

The accelerometer and *Ormia*-based sensor within their NB enclosure were then tested underwater using the NPS water tank in the sonar lab. The functional diagram and experimental setup are shown in Figure 31 and Figure 32, respectively. The test tank is two meters deep and the NB enclosure was placed one meter deep and separated one meter apart from an ElectroVoice UW30 underwater speaker. A Brüel and Kjaer Type 8103D100 calibrated hydrophone was positioned approximately 2 inches from the top of the NB enclosure (4 inches above the sensor's depth). The speaker was powered by an HP467A Power Amplifier and the hydrophone's signal was amplified by a Stanford Research Systems SR560 pre-amplifier (see Appendix C).

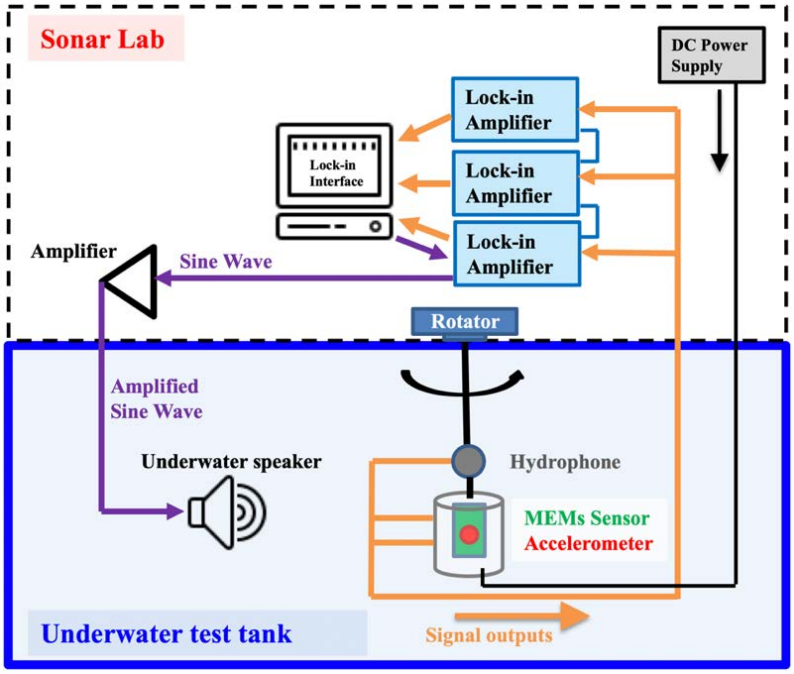

Figure 31. Underwater sensor characterization functional diagram

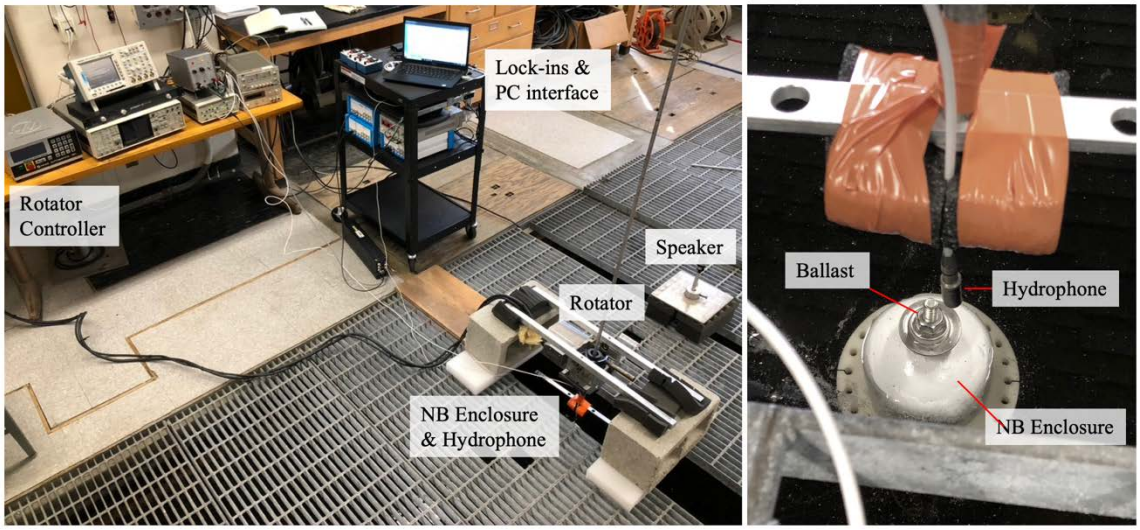

Figure 32. Underwater sensor characterization experimental setup

The NB enclosure was ballasted to be slightly negatively buoyant (to aid in stabilization) by adding mass (nut and washers) to the ballast bolt, as shown in the right-hand picture in Figure 32. The ballasting was achieved by placing the enclosure in the water, and adding or removing mass until the enclosure maintained a steady depth. Once a

neutral, steady depth was achieved, an extra 13 grams (2 washers) was added to make it slightly negatively buoyant.

1. Underwater Frequency Response

Since the goal is to characterize the sensor underwater, the characterization procedures from Section B(1) and (2) from this chapter were repeated. First, a frequency sweep was conducted to record the sensor's spectral sensitivity. The measured sound pressure near the location of the sensor is shown in Figure 33, as measured by the hydrophone (for sound pressure calculations, see Appendix C). Since the hydrophone's response is flat in this frequency range, this sound pressure level is effectively the acoustic stimulus at the sensor's location. The displayed sound pressure level does not distinguish between non-linearities in the underwater speaker, or effects of reflections from the tank walls and the water's surface.

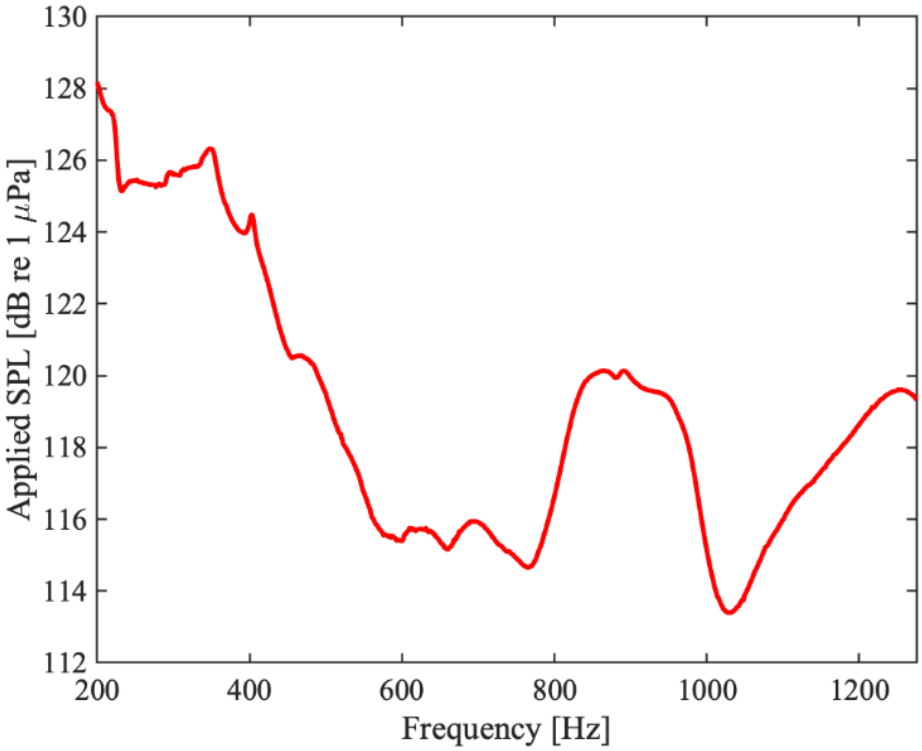

Figure 33. Measured sound pressure level using hydrophone

Figure 34 shows the sensitivity of the sensor in the 200–1275 Hz frequency range. The data is displayed in both mV/Pa and in dB re 1V/μPa for ease of analysis and comparison. Underwater resonant peaks were recorded at similar frequencies as in air (recall Figure 16). The peak at 692 Hz, is attributed to the sensor resonance. The peaks at 255 Hz and 1050 Hz are attributed to the PCB vibrations. This indicates that the main characteristics of this system did not change while underwater when operated in a neutrally buoyant configuration. As before, structural resonant peaks presented themselves beyond 1275 Hz, but for clarity they are omitted from the underwater frequency response curves. There is a noticeable decease in sensitivity between the sensor's response in air and underwater. Underwater, the peak sensitivity was 254 mV/Pa compared to in-air of 1.26 V/Pa. It is apparent that there are additional phenomena affecting the enclosure vibration underwater compared to in air. These differences can likely be attributed to forces caused by either drag, entrained water, or acoustic radiation effects on the underwater enclosure [27].

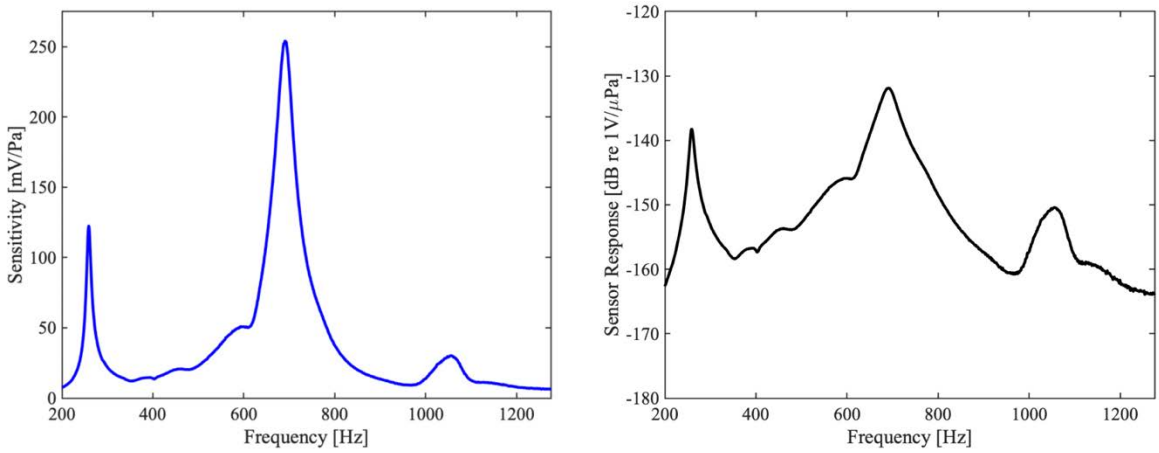

Figure 34. Underwater frequency response (6-1-2 sensor)

Figure 35 shows the accelerometer measurements of the PCB vibrations within the same frequency range (200-1275 Hz). To obtain this graph the accelerometer's output in Volts was converted to units of gravity, then divided by the pressure as recorded by the calibrated hydrophone. Familiar peaks at 259 Hz and 1035 Hz presented themselves as

they did in air, although the frequency of these peaks is approximately 1.5% different from that in air. The exact cause of the slight shift of resonant frequencies associated with the PCB requires further investigation.

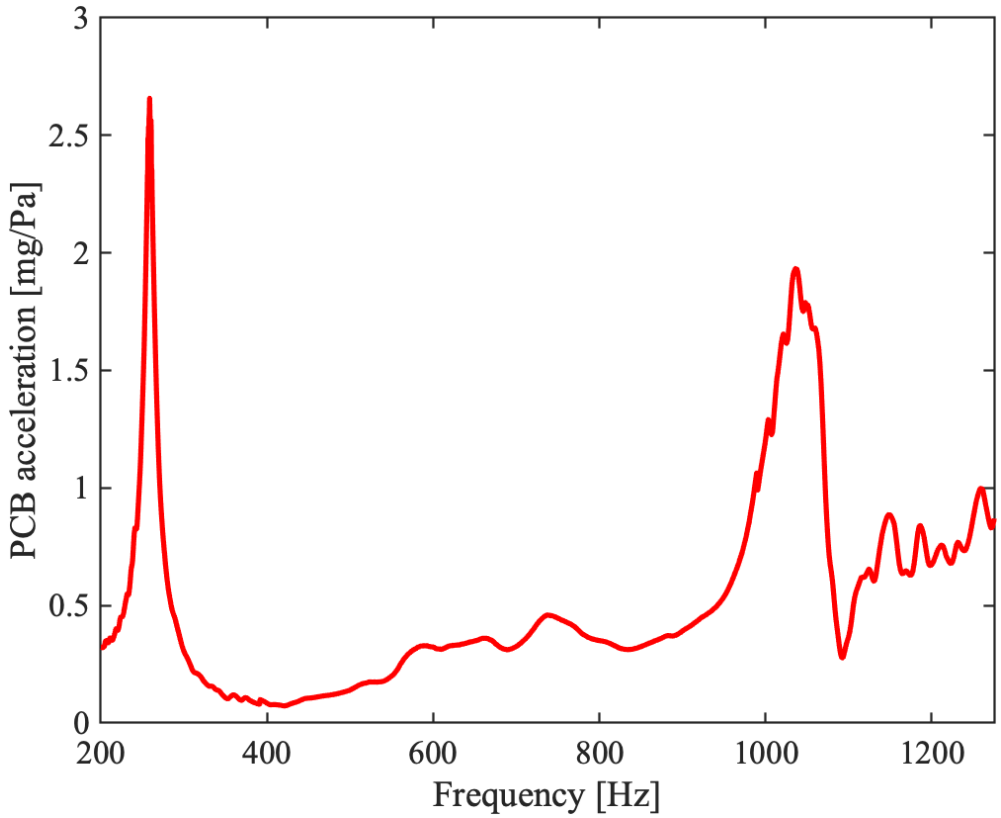

Figure 35. Underwater PCB acceleration (accelerometer)

It is possible to present the inertial sensitivity of the sensor in V/mg by dividing its response in V/Pa by the reference accelerometer's response in mg/Pa, as shown Figure 36. Like the sensor's response in air, which is presented on the same graph for comparison, the maximum response of the sensor occurred at its resonant frequency. In air, the peak sensitivity was 1.02 V/mg, and it reduced underwater to 0.81 V/mg. Ideally, the responses should be coincident; however, given that the accelerometer response was generally noisy, higher sensitivity accelerometer is needed to further quantify the differences between the sensor's underwater and in air acceleration sensitivity.

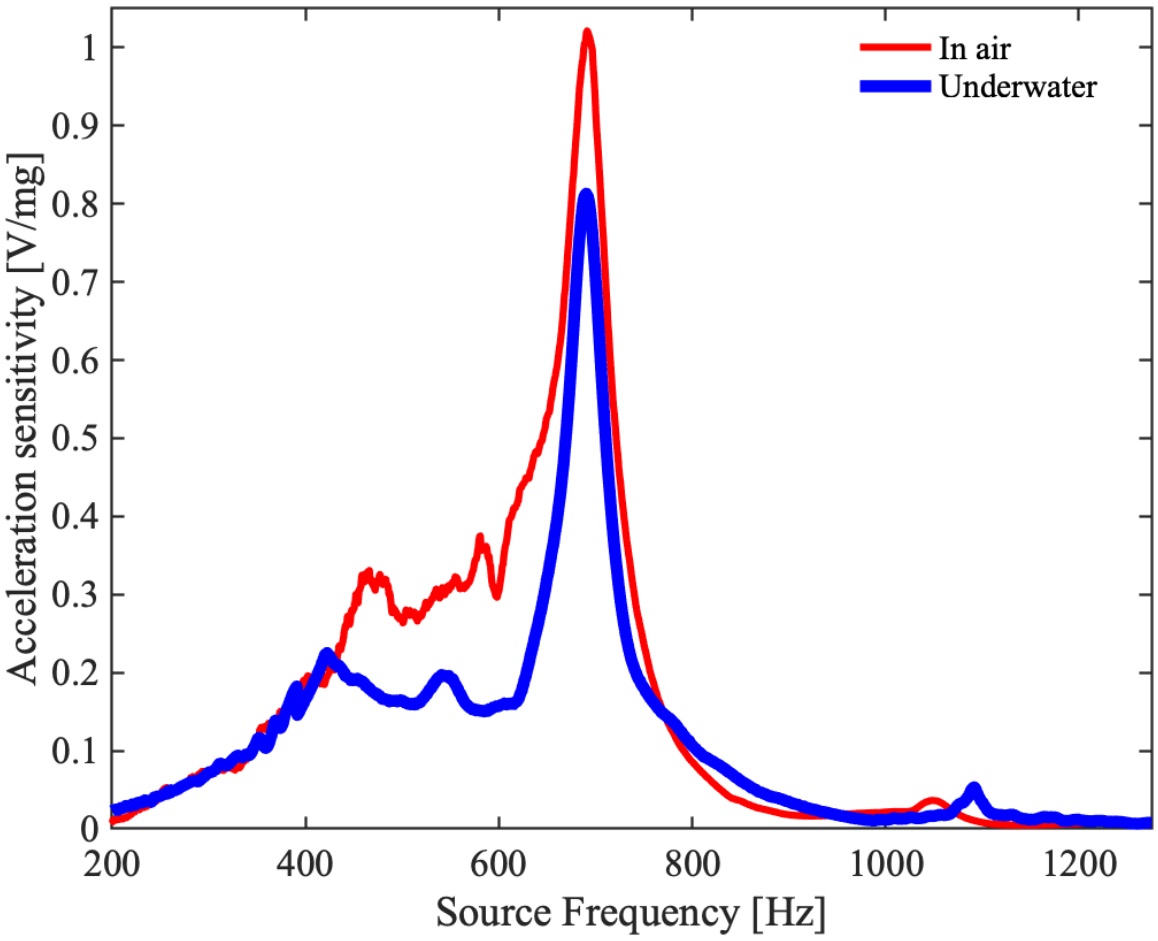

Figure 36. Underwater acceleration sensitivity (6-1-2 sensor)

Table 1 summarizes the sensor's peak maximum response for different units of measurements.

Table 1. Underwater sensitivity in NB configuration (6-1-2 sensor)

mV/Pa	**dB re 1V/µPa**	**V/mg**
254	-131.9	0.81 V/mg

The sensitivities given are all taken at the sensor's resonant frequency of 692 Hz. The sensor's output was normalized against the calibrated hydrophones and accelerometer's response.

2. Underwater Directional Response

Once again, the sensor and accelerometer's directional responses were measured by sending a single tone to the underwater speaker while rotating the NB enclosure using a Haas HA5C rotator with a Haas Brushless Rotary Servo Control. The excitation frequency for the directional tests was at the sensor's resonance of 692 Hz.

The directional response measurements were taken at several rotation rates, however only the response at 0.5 degrees per second is shown in Figure 37. Both the accelerometer's and sensor's directional responses are shown in a cartesian and polar plot in Figure 37. The ripple across the sensor's directional response is due to vibration induced by the rotator and it was observed for all rotation speeds. The rotator's motor noise was confirmed as the source of the noise by recording the sensor's directional response with the speaker turned off. The sensor showed similar ripple resulting from the rotator.

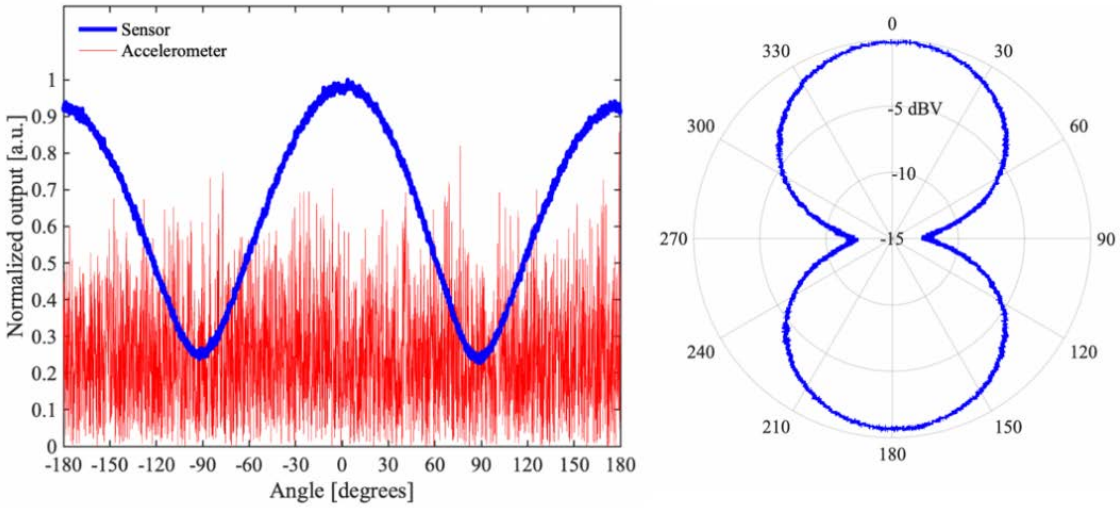

Left: the sensor and accelerometer's directional measurements in which both devices outputs were normalized by their maximum output. Rotation speed: 0.5˚/second. Right: the same data displayed in a polar plot in units dBV, and the maximum device voltage was normalized to 0 dBV.

Figure 37. Underwater directional response at 692 Hz (6-1-2 sensor and accelerometer)

In general, the sensor's directional response magnitudes were the same for all rotation speeds, resulting in approximately -13 dBV of attenuation off-axis at 90˚. Compared to the in-air cross-axial sensitivity of -18 dBV (recall Figure 19), the underwater directionality decreased. Considering that in some tests (recall sensor 6–1-3's directional response in Figure 29 and Figure 30), better than -30 dBV cross-axial sensitivity was achieved, there are sources of error that significantly affect the directional measurements. These errors may be attributed to mechanical coupling between the acoustic source and the sensor, reverberation effects from the tank, asymmetric hanging of the NB enclosure from its support bar, etc. Further experimentation is required to verify the source of these errors. The accelerometer's response was too low to show any directionality.

3. Underwater Linearity Tests

In order to determine if the linearity of the sensor's response would be different underwater than in air, the sensor's output was measured at a constant frequency (692 Hz) with a discreet set of sound pressures. Voltage supplied to the speaker was held steady for enough time to record the hydrophone, sensor and accelerometer's responses, and the speaker voltage was subsequently lowered in steps. To generate a plot of the sensor's linearity normalized to PCB acceleration, the mean of both the sensor and accelerometer's output were calculated over each time interval for which the sound pressure was held steady, as shown in Figure 38. As expected, both the sensor and accelerometer responses decrease with the reduction in pressures, although only the sensor shows the discrete steps. The standard deviation of the accelerometer's response over each region was also calculated and plotted as error bars.

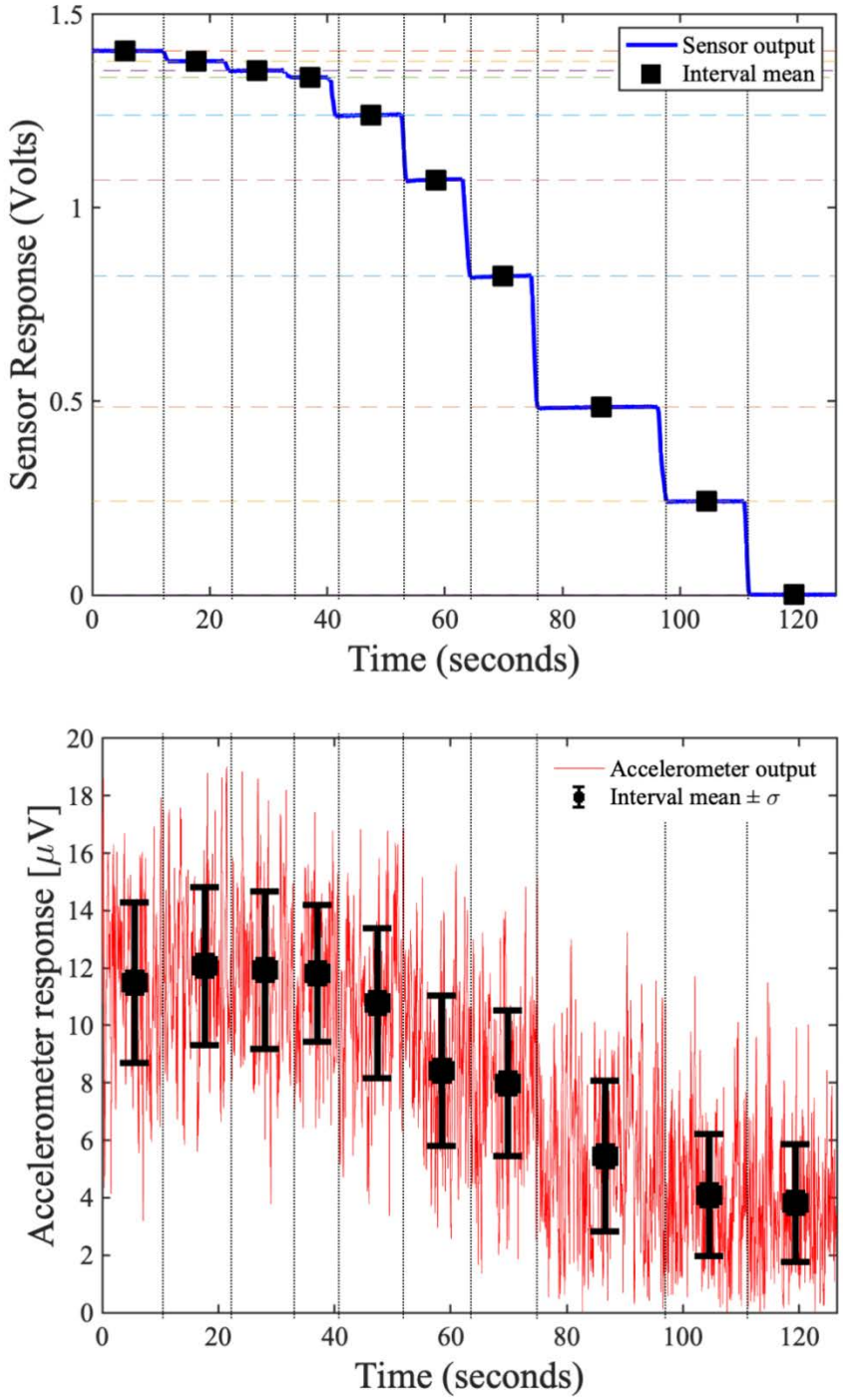

Top: The speaker's excitation was lowered in stages, as represented by the corresponding steps in the sensor's response. The sensor and accelerometer mean responses over each time stage were taken for each region, as represented by the black squares. Bottom: Due to the accelerometer noise, error bars represent the standard deviation of the accelerometer's response.

Figure 38. Sensor and accelerometer underwater response for various excitation pressures at 692 Hz

For each region, mean values of the signal were computed for both the sensor and accelerometer. Figure 39 shows the sensor signal versus acceleration at different sound pressures along with a linear fit. The red line represents sensitivity (V/mg) of the sensor obtained from the sensor's response in air at 692 Hz in Figure 18. It is expected that if the accelerometer had a better resolution and sensitivity, then the sensitivity (V/mg) measured underwater in the NB configuration would exhibit a linear response with a slope closer to 1.2 V/mg.

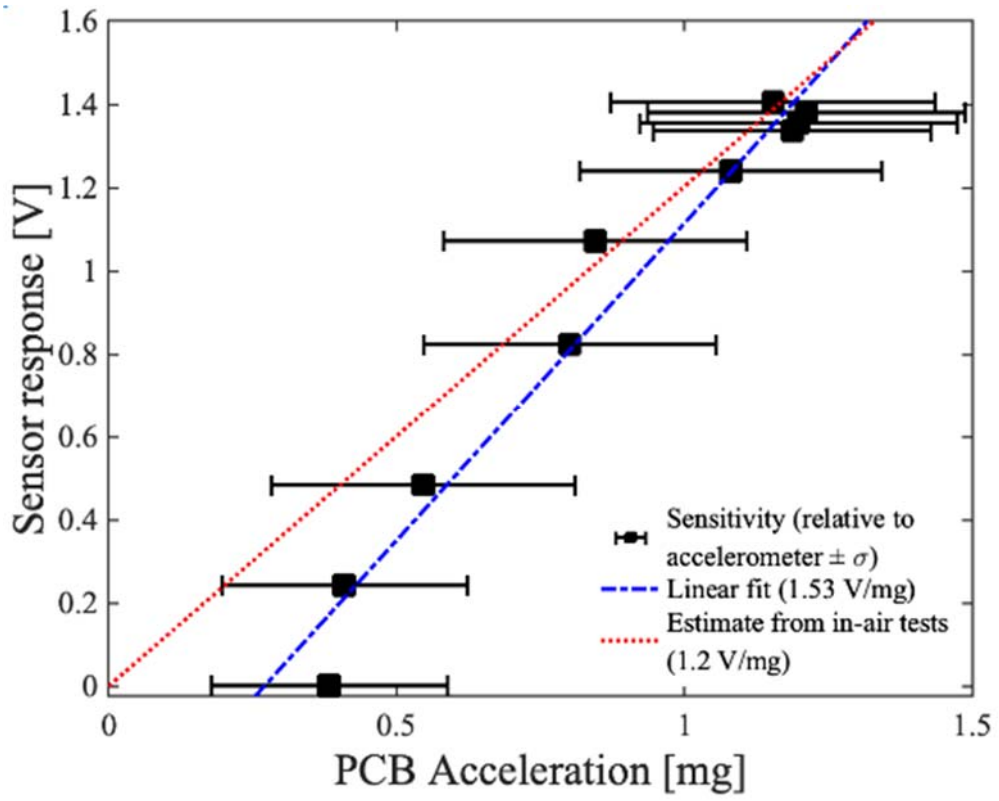

The 6-1-2 sensor was normalized against the reference accelerometer while both were excited at discrete sound pressures at 692 Hz.

Figure 39. Underwater linearity test of 6-1-3 sensor (accelerometer reference)

Figure 40 shows the sensor voltage plotted against the pressure as measured by the hydrophone for the same linearity test. The sensor operating underwater in the NB configuration exhibited a linear response just as it did in air (Figure 13) with a sensitivity of 0.26 V/Pa. It is important to notice that the sensitivity for underwater operation is about

20% of the estimated sensitivity for in air operation, which is shown in red. The estimated sensitivity of 1.26 V/Pa is the peak sensitivity taken from the in-air frequency sweep shown in Figure 16 on page 27. This decrease in sensor sensitivity is likely due to higher viscous forces on the enclosure, preventing it from moving as much as it does in air [27].

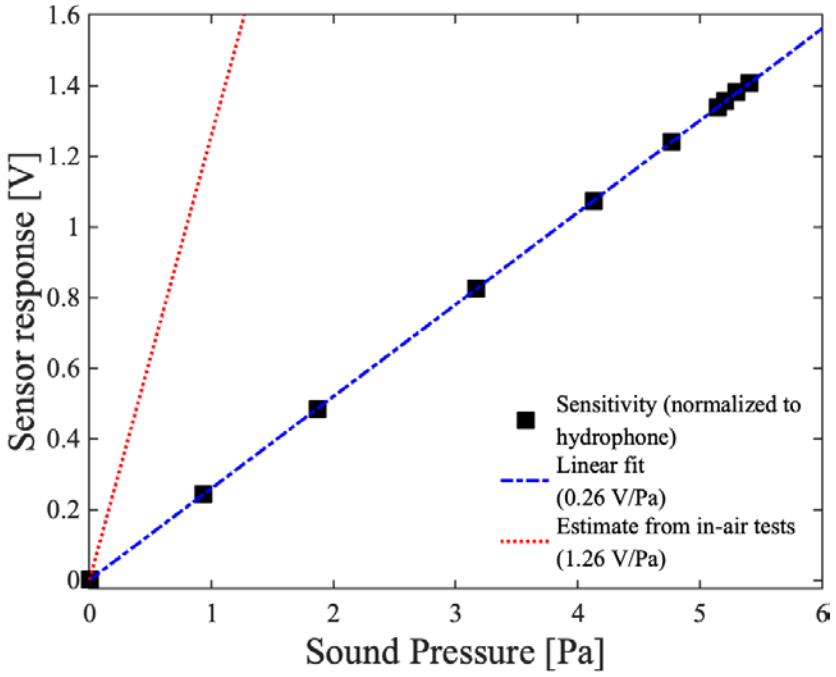

The 6–1-2 sensor was normalized against the reference hydrophone while both were excited at discrete sound pressures at 692 Hz.

Figure 40. Underwater linearity test of the sensor (hydrophone reference)

D. SIGNAL-TO-NOISE MEASUREMENTS

The noise spectral density (NSD) of the sensor was measured in the anechoic chamber to determine its noise performance as well as to determine the signal-to-noise ratio. The MFLI and LabOne software were used to measure the noise in accordance with the settings in Appendix E. Figure 41 shows the noise spectral density of the 6–1-3 sensor. The NSD rolls off in the low frequencies because there is an active high pass filter on the sensor readout electronics board with a cutoff frequency of 300 Hz. The noise is predominantly from the readout electronics [41]; however, the two humps between 600

and 800 Hz are most likely due to intrinsic mechanical noise (thermal agitation) of the sensor associated with its fundamental modes.

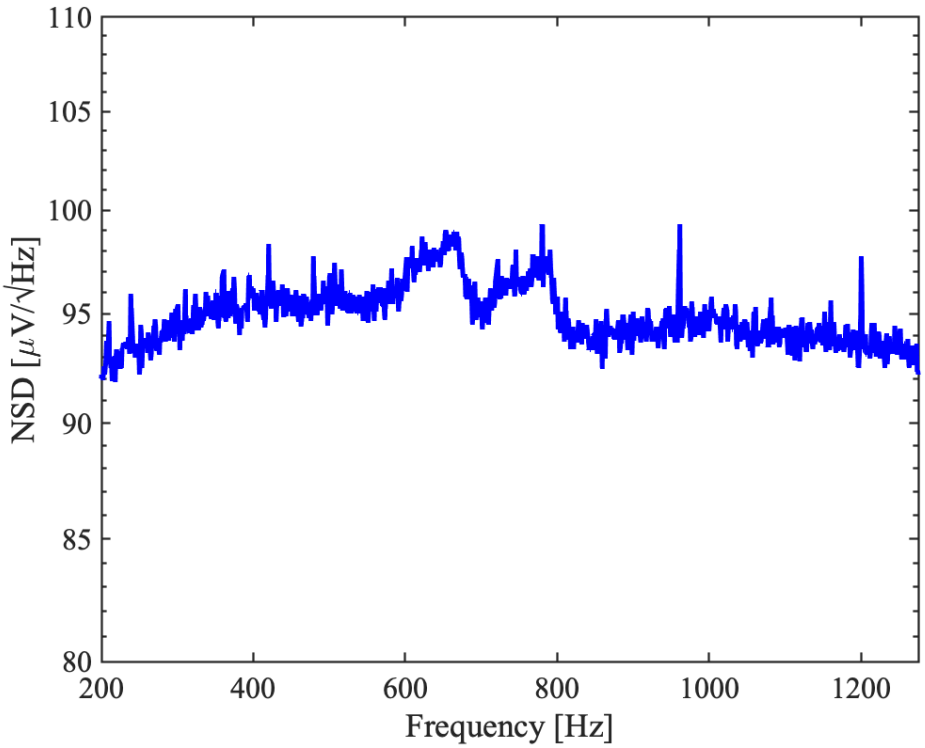

Figure 41. Noise spectral density (6-1-3 sensor)

Although the NSD result is for 6–1-3 sensor, it is of the same family as the sensor that was tested underwater, 6–1-2. The 6–1-2 sensor was damaged before NSD measurements were completed. Applying 6–1-3's NSD measurements to 6–1-2's underwater frequency response, we can determine the signal-to-noise ratio, expressed in dB as

$$SNR_{dB} = 20\log_{10}(\frac{V_{signal}}{V_{noise}}), \quad (4.1)$$

where V_{signal} is the output of the sensor in Volts when the sound stimulus is 1 Pa at all frequencies, and V_{noise} is the total noise between the desired frequency bandwidth. The total noise, V_{noise} , is given by

$$V_{noise} = \sqrt{\int_{f1}^{f2} NSD^2 df}\,, \tag{4.2}$$

where f_1 and f_2 are the frequency limits in Hertz, and the NSD is the noise spectral density measured in Figure 41. Applying equation 4.2, Figure 42 presents the sensor's underwater signal to noise ratio from 200–1275 Hz. The SNR shows a local maximum at 255 Hz (31 dB) and a global maximum at 692 Hz (37 dB).

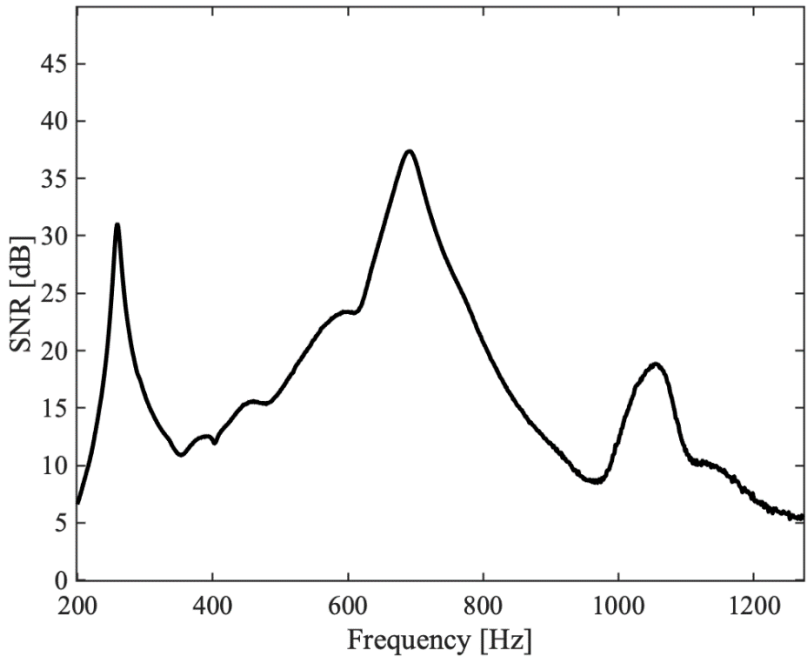

The signal to noise ratio represents a sensor signal excited by 1 Pascal.

Figure 42. Underwater signal-to-noise ratio (6-1-3 sensor)

The dynamic range of the sensor, which is the "ratio between the highest and the lowest detectable signal levels" [48], is defined as

$$DNR_{dB} = 20\log_{10}\left(\frac{V_{max}}{V_{noise}}\right), \tag{4.3}$$

where V_{max} is the maximum voltage output in which the sensor responds linearly. Considering a $V_{max} = 4.5\,Volts$ [58], and $V_{noise} = 3.44 * 10^{-3}$ (previously calculated over 200–1275 Hz from Equation 4.2), the sensor's dynamic range (DNR) is $62.3\,dB$.

THIS PAGE INTENTIONALLY LEFT BLANK

V. CONCLUSION

A. SUMMARY

A biomimetic, directional, MEMS acoustic sensor designed to operate near resonance with capacitive-based readout was demonstrated to operate underwater in a neutrally buoyant configuration. Many previous studies on sensors that mimic the hearing organ of the parasitoid fly *Ormia ochracea* focused on detecting and localizing sound by exposing the sensor directly to oscillating particles from an acoustic pressure wave. Investigating a different approach to sound detection with *Ormia*-based sensors, this work's objective was to determine if it was possible to measure the acceleration of a neutrally buoyant enclosure whose movement was under oscillatory motion as a result of the pressure force from an acoustic wave. This study demonstrated through various experiments that the NPS-developed MEMS sensor can operate in a neutrally buoyant configuration.

A neutrally buoyant enclosure and a sensor mounting system was designed and fabricated, and experimentation was conducted to characterize the sensor's frequency response, sensitivity and directionality, both in air and underwater. The obtained results support the answers for the three posed research questions as follows:

Will the MEMS sensors maintain the same characteristics in a NB configuration as in air?

The inherent operation of the sensor does not change when sensing the underwater enclosure acceleration. The acceleration sensitivity in [V/g] is nearly coincident in air and underwater. The pressure sensitivity in [V/Pa] measured underwater is only about 20% of the measured pressure sensitivity in air due to the differences in viscous forces between the two media. The frequency response of the sensor-enclosure system exhibits extra resonant peaks when compared to the frequency response of the sensor. This was proven to be due to the natural vibrational modes of the enclosure and vibrational interaction with the mounting

system; however, the frequency responses of the sensor-enclosure assembly in air and underwater show a good match.

Is it possible to test directionality of a neutrally buoyant configuration using NPS facilities?

All in-air characterizations were conducted at the NPS acoustic anechoic chamber, which were adequate in terms of the absorption and noise floor characteristics. In addition, the instrumentation included high-end lock-in amplifiers and calibrated microphones, which assured repetitiveness and accuracy.

All underwater experiments were conducted at the NPS sonar lab water tank. The measurements showed good repetitiveness despite the tank's small size when compared to the wavelengths of interest. Although mechanical coupling between the acoustic projector and the device under test were minimized by several dampeners, the effects of wall and surface reflections still need to be further investigated.

What are the characteristics of a NB MEMS sensor assembly and how do they compare with other sensor technology that is designed to detect and localize underwater sound?

The main figures of performance of the neutrally buoyant assembly can be summarized as:

(a) Sensitivity at resonance (692 Hz): 0.81 V/mg (-131.9 dB re 1V/μPa); sensitivity off-resonance (400-600 Hz): 0.18 V/mg (-157 to -146 dB re 1V/μPa); and sensitivity off resonance (>900 Hz): 0.01 V/mg (-160 dB re 1V/μPa).

(b) Signal to noise ratio (for 1 Pa signal) at resonance (692 Hz): 37 dB

(c) Noise spectral density (200-1275 Hz): ~ 95μV/$\sqrt{}$Hz

(d) Dynamic range (200-1275 Hz): 62.3 dB

(e) Directionality: dipole pattern with ~13 dB cross-axial sensitivity.

These results are comparable to those obtained in similar research with a peculiarity that the *Ormia*-based MEMS sensors are designed to operate at their natural frequencies to maximize performance in specific applications. Although the sensor is operating at resonance and its frequency response is not flat, this characteristic could be exploited for situations that do not require high sensitivity across the full frequency spectrum. Such specially designed narrow-band detection schemes with the Navy's Sound Surveillance System (SOSUS) were exploited as early as the 1970s [1].

Experiments completed at NPS yielded promising results in both spectral sensitivity and directionality measurements. The results offer improvements, both in sensor size and performance, when compared to previous underwater tests at NPS using the same sensor. Addressing the needs of the Navy, a nascent miniature sensor capable of detecting the intensity of sound with inherent directionally may prove valuable for gaining a scalable technological advantage in the undersea acoustic domain.

B. RECOMMENDATIONS FOR FUTURE WORK

Follow-on work studying *Ormia*-based MEMS sensors in a neutrally buoyant configuration may offer improvements in enclosure design, sensitivity, and directional responses.

Enclosure design improvements may simplify the analysis of frequency response and directionality measurements. Although the enclosure design presented in this work is economical and easy to fabricate, the complex asymmetries can be improved in order to limit any interference between the enclosure and the surrounding water. Ideas to improve the design include fabrication using a specially designed syntactic foam, ceramic, or moldable plastic. This could allow for integration of multiple parts into one complete structure, be it cable penetrations, ballasting systems, sensor board mounts, or stabilization strings. The stabilization strings could be improved by incorporating a greater ability to adjust the length of the strings, as well as possibly testing a four-string design. Structural resonances should be minimized by ensuring an even greater rigidity between the sensor board and the enclosure. Ballasting could be improved by using a low-melting point metal to add ballast inside of the enclosure instead of outside, although this is a more difficult process.

Another improvement which is already underway is the miniaturization of the sensor's electronics board. Although the demonstrated enclosure could have been made smaller with the current sensor board, further miniaturization would allow for an even smaller enclosure compared to the wavelength of sound. This may lead to increased sensitivity and more accurate measurements as a result of reducing viscous drag forces and ensuring lateral field uniformity [27]. One disadvantage of miniaturizing the enclosure is that for a deployable sensor, a smaller enclosure will likely result in larger amounts of noise caused by hydrodynamic flow, since the *Ormia*-based sensor is extremely sensitive to motion and all sources of noise [29]. Additional improvements to the sensor's readout electronics should be considered in order to lower the sensor's electronic noise, either by reducing the onboard gain or by other means.

If improvements to the enclosure and PCB mounting design eliminate structural resonances, directionality measurements should be conducted at multiple frequencies rather than just at sensor resonance. It is hypothesized that the *Ormia*-based sensor will maintain its inherent directional response at all frequencies so long as the vibrational modes are not influencing the response as demonstrated in this thesis.

Regarding equipment choices, it is recommended that a more sensitive accelerometer in the frequency range of interest is used. The accelerometer used in this thesis's experiments had the advantage of being lightweight with a small footprint, but the sensitivity was inadequate in order to collect clean measurements. Additionally, a special cable should be acquired that is thin, flexible, and has a waterproof jacket. The sensor's cable that was used for all experiments was a four-conductor, 32 AWG cable with a non-waterproof jacket. It is suspected higher pressure environments may cause compression of the jacket and subsequent water intrusion via the enclosure penetrations.

Finally, since the current directional response is a dipole, there is still bearing ambiguity. This ambiguity could be resolved by restricting the backside cavity, or by using a canted angle sensor design. Either of these detection schemes could be implemented in the same enclosure used in this study.

APPENDIX A. MICROPHONE CALIBRATION AND PRESSURE CALCULATIONS

The reference microphone system was a 1/2" element PCB 378A21 microphone with PCB 426E01 pre-amplifier. The microphone's signal passed through a PCB 482C Signal Conditioner with 100 times gain.

To calibrate the system, a Larson Davis CAL200 Handheld Sound Level Calibrator output 94 dB (1 Pascal) onto the microphone at 1 kHz. This one pascal of pressure excites the microphone and the microphone's voltage was then measured at 1 kHz on the MFLI. This number was recorded as the $Sensitivity_{System}$ in V/Pa and was typically on the order of 1.1 V/Pa. The applied pressure is then determined by

$$Pressure\ (Pa) = \frac{V_{mic}}{Sensitivity_{System}},$$

where V_{mic} is the output of the microphone in RMS voltage measured after its 100 times gain signal conditioner. The sound pressure in dB is defined as

$$SPL_{dB\ re\ 20\ \mu Pa} = 20\log_{10}\left(\frac{V_{mic}}{Sensitivity_{System} * P_{ref}}\right),$$

where $P_{ref} = 20\ \mu Pa$ [59].

THIS PAGE INTENTIONALLY LEFT BLANK

APPENDIX B. ACCELEROMETER SETUP, CALIBRATION, AND NORMALIZATION

The Endevco Model 22 accelerometer does not have an onboard charge to voltage converter, and as such its output must pass through the Meggitt 2775A signal conditioner. From the manufacturer's manual [60], the acceleration in units of gravity is calculated based off of the system sensitivity in Volts/g given by

$$Sens_{System} = \frac{Full\ Scale\ Output\ (V_{Pk})}{Full\ Scale\ Range\ (g_{Pk})},$$

where the full-scale output is 0.9956 V (set by the 2775A AC ADJ Pot) and the full-scale range is set to 100 g. The acceleration measured by the accelerometer follows

$$g\ (engineering\ units) = \frac{V_{accel}}{Sens_{sytem}},$$

where V_{accel} is the RMS voltage of the accelerometer as read on the MFLI.

The settings of the 2775A signal conditioner for all tests are shown in the following table.

Full scale range	*100*
Mode switch	*OP*
Filter	*IN*
Input	*Gnd*
Lo Freq	*<1 Hz*
Multiplier	*0.1*
Sensitivity [pC/g]	*4.90*

THIS PAGE INTENTIONALLY LEFT BLANK

APPENDIX C. UNDERWATER CALIBRATION, SENSITIVITY, AND PRE-AMPLIFIER SETTINGS

The B&K Type 8103 hydrophone has a flat response over all frequencies tested in this thesis, and its calibrated sensitivity is 22.3 μV/Pa. The 8103 hydrophone's output was conditioned by a Stanford Research Systems SR560 pre-amplifier with 1000 times gain applied. The calculation for the sound pressure follows

$$Pressure\ (Pa) = \frac{(V_{hyd}/1000)}{Sensitivity_{System}},$$

where V_{hyd} is the voltage output of the hydrophone as read on the MFLI (includes 1000x gain) and the $Sensitivty_{System}$ is 22.3 μV/Pa (based on the hydrophone calibration). The sound pressure level in units of dB re 1 μPa is

$$SPL_{dB\ re\ 1\ \mu Pa} = 20\log_{10}(\frac{Pressure}{P_{ref}}),$$

where $P_{ref} = 1\ \mu Pa$. The sensitivity of the hydrophone in units of dB re 1 μPa is

$$Sensitivity_{dB\ re\ 1\ \mu Pa} = 20\log_{10}(\frac{Sens_{Pressure}}{1V/\mu Pa}),$$

where $Sens_{Pressure}$ is the pressure sensitivity of the sensor in units of V/μPa.

The settings for the SR560 pre-amplifier are shown in the following table.

Low-pass filter	*OFF*
High-pass filter	*OFF*
Coupling	*AC*
Invert	*OFF*
Gain mode	*Low Noise*
Gain	*1x10^3*

THIS PAGE INTENTIONALLY LEFT BLANK

APPENDIX D. TURNTABLE INFLUENCE ON NSD

Since the rotational directional response data exhibited noisy signals uncharacteristic to other *Ormia*-based sensors with higher resonant frequencies, it was important to research the source of the excess electronic noise. To test this, the 6–1-3 was placed in its mount and on the rotator as shown in Figure 43, and the NSD was measured for three different conditions with the speaker OFF (no sound excitation). The first condition was measuring the NSD with the turntable on but not rotating, and no accelerometer on the PCB. The second was with turntable rotating at 1˚/second, also without the accelerometer on the PCB. The final condition was the turntable rotating, but this time with the accelerometer placed on the PCB.

Figure 43. Turntable influence on noise spectral density (6-1-3 sensor)

Figure 44 shows the influence of the turntable on the sensor's response with a significant vibration at 375 Hz and the associated harmonic frequencies of this vibration. Even with the turntable on but not turning, the sensor senses the extra noise (the NSD from

Curve 1 is greater than the NSD shown on page 52). Adding mass to the PCB (in the form of the accelerometer) shifted the resonances and their harmonics to higher frequencies (Curve 2 is shifted to the right from Curve 3). Since removing the accelerometer from the PCB shifts the frequency of vibration, this indicates that the PCB and its mount is undergoing some form of pendulum action when under the influence of an acoustic pressure wave. It is noted that the sensitivity of the accelerometer is not great enough to show a significant difference in its NSD between any of these three tests --its response was at its noise floor. The unlabeled curve was rotation without the mass at the accelerometer, but the rotation rate was higher faster than Curve 3.

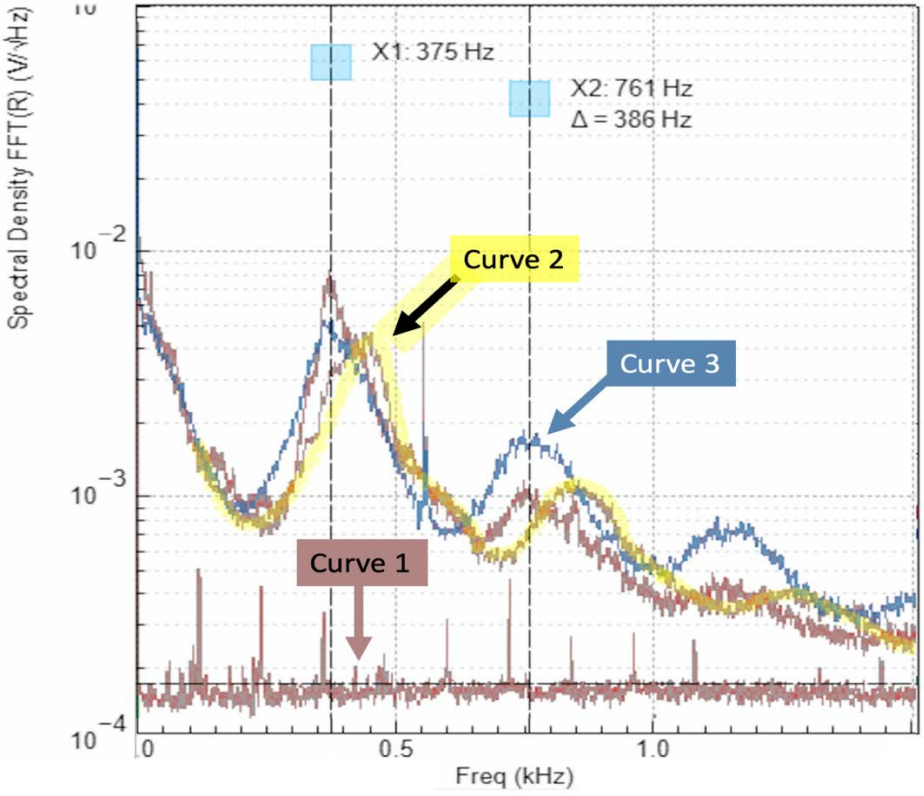

Curve 1 is the NSD of the sensor with no sound stimulus and with the rotator turned ON but not rotating. Curve 2 is the sensor response with the turntable turning (1˚/second) and the accelerometer placed on the PCB. Curve 3 is the sensor's response with the turntable turning and the accelerometer removed.

Figure 44. Turntable influence on noise spectral density (6-1-3 sensor)

APPENDIX E. MFLI NSD MEASUREMENT SETTINGS

The following LabOne software settings were used for the NSD measurements.

Lock-In tab	**For each device**	Signal Input	Coupling	*AC*
			Range	*AUTO*
		Low Pass Filter	Order	*1*
			BW 3dB	*8000 Hz*
		Data Transfer	PC	*ENABLED*
			Trigger	*Enabled/continuous*
		Reference Frequency	*8000 Hz*	
Spectrum tab	**Control tab**	Horizontal	Frequency Span	*16 kHz*
			Refresh Rate	*5Hz*
			Spectral Density	*Enabled*
		Vertical	Signal Type	*Demod R*
			Signal	*Demod 1 Sample Spec Dens FFT (R)*
	Settings tab	FFT	Length	*16,384*
			Window	*Hann*
		Grid Settings	Rows	*1*
			Averages	*10,000*
			Waterfall	*ENABLED*
			Overwrite	*ENABLED*
		Display	Plot type	*ROW*
			Palette	*Default*
			Mapping	*Log*
			Scaling	*Auto*

THIS PAGE INTENTIONALLY LEFT BLANK

APPENDIX F. ENCLOSURE VIBRATIONAL MODES

Another sensor from the same family, 6–1-3, was placed in the NB enclosure and three different frequency sweeps were performed. First, a frequency sweep without extra mass on the upper endcap. Second, a frequency sweep was performed with 66.6 g of mass added to the ballast bolt on the upper endcap. Third, the 66.6 g mass was removed and the support bar was rotated so that it was on-axis with the direction of sound propagation, as shown in the top right of Figure 15.

The first and third tests show that the effect of changing the orientation of the support bar exhibited little difference in the sensor's normalized sensitivity response, as shown in Figure 45. The green curve represents this third test and the sensor's response is nearly identical at sensor resonance. This is important because it eliminates the effect of the support string orientation on both frequency response tests.

The second test proved that the sensor's sensitivity was doubled when the extra mas was added to the ballast bolt (see the detailed view in Figure 46). Although the exact mechanism causing this difference requires further investigation, it is hypothesized that when the mass is added, the center of mass of the enclosure was raised to approximately the top third of the enclosure, which is also the approximate location of the sensor inside. As a result, it is suspected that a shift in the enclosure center of mass influences possible changes in torque about stabilizing ring when the acoustic wave imparts its pressure on the shell.

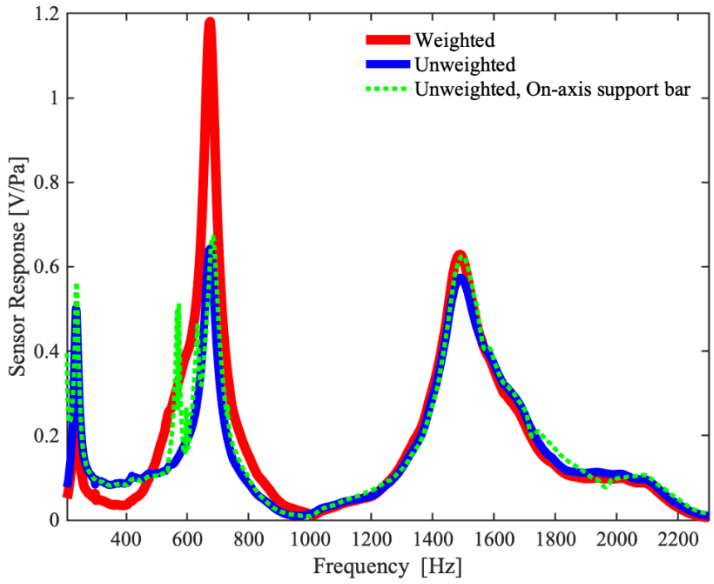

Figure 45. In-air (NB enclosure) frequency response with various testing conditions (6-1-3 sensor)

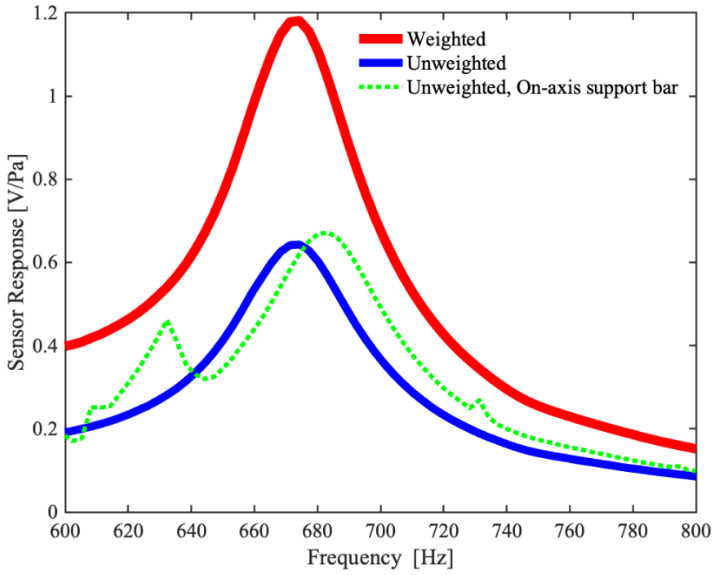

This figure is a detail view from 600–800 Hz of the data presented in Figure 45

Figure 46. Detail view of in-air (NB enclosure) frequency response at sensor resonance

The effects of the extra 66.6 g mass on the ballast bolt as well as the support bar orientation was further investigated by studying the accelerometer's response on the outside of the enclosure. A frequency sweep from 200–2300 Hz was conducted for various testing conditions. With the accelerometer placed both on the back and on the side of the enclosure, in Figure 47, the frequency sweep was conducted for different conditions of ballasting weight and support bar orientation.

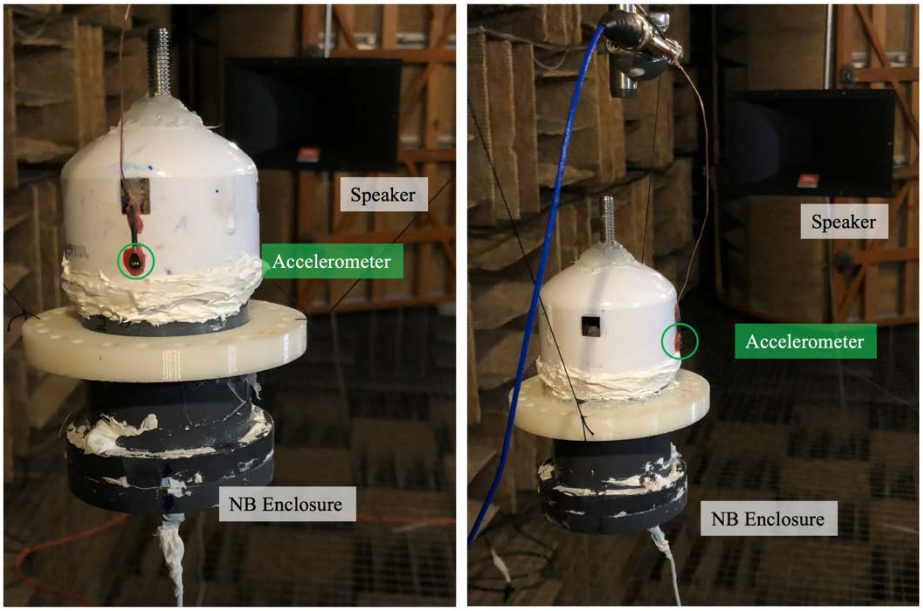

The left photo shows the accelerometer on the back of the enclosure, while the right photo shows the accelerometer on the side. image shows the accelerometer at various locations on the NB enclosure. The top left photo is the accelerometer placed on the mirror. The large photo on the right shows the accelerometer placed on the side of the enclosure.

Figure 47. Enclosure vibrational response experimental setup (accelerometer)

Figure 48 shows the enclosure vibration for these frequency sweeps as measured by the accelerometer. The green curve represents the accelerometer on the back of the enclosure and no extra mass added to the ballast bolt, and the support bar was oriented perpendicular to the direction of acoustic wave propagation. The solid red line represents the enclosure vibrations with the accelerometer on the back, with 66.6 g added to the ballast bolt. Removing the 66.6 g and moving the accelerometer to the side, the vibrational response was recorded and is shown in the red-dashed line. The solid blue line shows the

effect of rotating the support bar 90˚ and no extra mass added. With the support still at 90˚ and without mass, the accelerometer was moved to the side and once again the frequency response was measured and is shown by the dotted blue line.

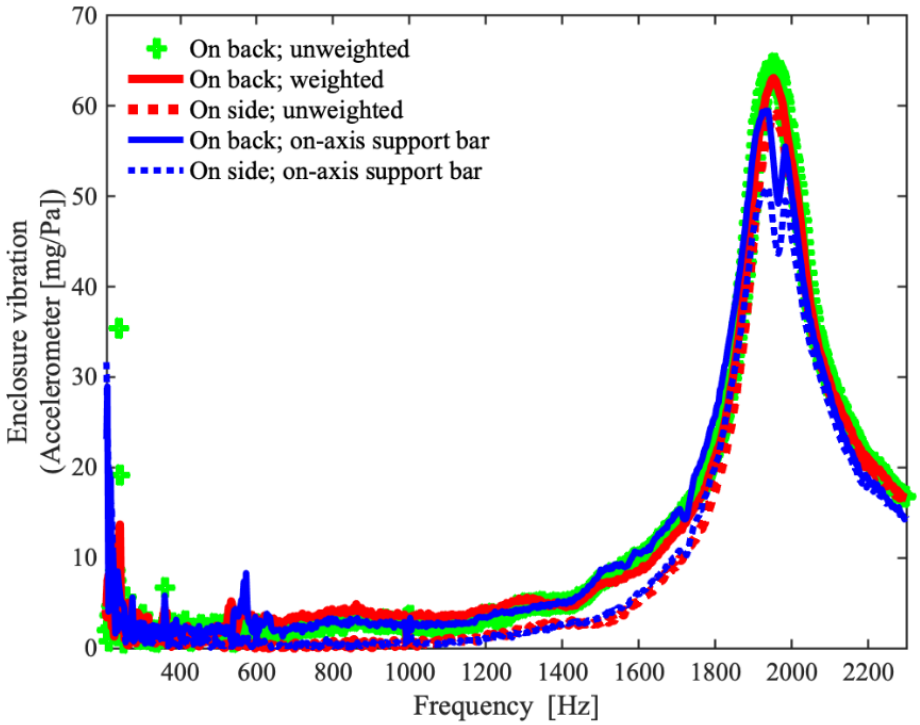

"On back" and "on side" refers to the accelerometer's position on the enclosure relative to the speaker's position. "On side" is at the same vertical position on the enclosure, but rotated 90˚ on the enclosure.

Figure 48. Effects of weight and support bar orientation on enclosure vibrational response (accelerometer)

The enclosure vibrational response as a function of frequency reveals a strong vibrational peak at 1950 Hz and no peak 1490 Hz, further indicating that peaks between 1400–1500 Hz are from the PCB or PCB mount, and not the enclosure. Since the peak at 1950 Hz correlates with the data in Figure 26, and there was a significant vibrational response for all positions of the accelerometer, the enclosure itself is further verified to be experiencing a vibrational mode. If the enclosure was not experiencing a structural mode at 1950 Hz, the accelerometer would have a minimal response when positioned on the side of the enclosure. Additionally, it is shown that the support bar orientation does influence

the vibrational mode of the structure at 1950 Hz, but the vibrational mode is still present. Although the sensor's directional response at its resonant frequency is not influenced by the support bar orientation (recall Figure 29 and Figure 30), further experimentation underwater is required to characterize the sensor's directional response across the full frequency spectrum.

THIS PAGE INTENTIONALLY LEFT BLANK

APPENDIX G. BUOYANCY CHARACTERISTICS OF THE NB ENCLOSURE

To quantify the buoyancy characteristics of the NB enclosure, the enclosure and its parts were weighed on a laboratory scale as shown in Table 2. The component volumes were recorded by observing the amount of water displaced when the enclosure and parts were submerged in a beaker. The volume of cabling was estimated by a cylindrical volume calculation based on the diameter of the accelerometer signal cable (1.5 mm) and sensor cable (2.0 mm) based on 1 meter of submerged cabling.

Table 2. Mass and fluid displacement of the NB sensor system

Component	Mass (g)	Volume (cc)[a]
PVC enclosure[b]	443.3	470
Ballast (nuts and washers)	24.55	23.5
Cabling	11.15	4.9
Sensor, accelerometer, and sensor mount	37.28	-
Total	517.3 (cc)[c]	498.4

[a]Volume of the displaced fluid.

[b] The mass and volume of NB enclosure, its endcaps, ballast bolt, hot-melt glue, and permanently installed cables were measured as one hole unit

[c] Based off the density of water at 20˚C = 0.998g/cc

Due to the capacity graduation width on the beakers, the volume measurements are estimates to within approximately 2%. In practice, the amount of ballasting required was determined by placing the assembled enclosure in the water, and then ballast (nuts and washers) was added in order to achieve the desired buoyancy. In order to maintain a relatively stable enclosure position underwater, the enclosure was ballasted to be negatively buoyant by approximately 10 grams.

THIS PAGE INTENTIONALLY LEFT BLANK

LIST OF REFERENCES

[1] D. Owen, *Anti-Submarine Warfare*, Barnsley, UK: Seaforth Publishing, 2007.

[2] R. C. Manke, Overview of U.S. Navy Antisubmarine Warfare (ASW) Organization During the Cold War Era, Newport, RI, USA: U.S. Naval Undersea Warfare Center, Newport Division, 2008.

[3] Congressional Research Service, "China naval modernization: Implications for U.S. Navy capabilities," Congressional Research Service, Washington, DC, USA, CRS Report No. RL33153, 2020.

[4] Congressional Research Service, "Navy Force Structure and Shipbuilding Plans: Background and Issues for Congress," Congressional Research Service, Washington, DC, USA, CRS Report No. RL32665, 2020.

[5] R. Holler, "The Evolution of the Sonobuoy from World War II to the Cold War," *U.S. Navy Journal of Underwater Acoustics*, January, 2014.

[6] C. Sherman and J. Butler, *Transducers and Arrays for Underwater Sound*, New York, N.Y., USA: Springer, 2007.

[7] FAS, "Military Analysis Network," 12 December 1998. [Online]. Available: https://fas.org/man/dod-101/sys/ship/weaps/an-sqr-19.htm.

[8] FAS, "Intelligence Resource Program," 6 July 1999. [Online]. Available: https://fas.org/irp/program/collect/surtass.htm.

[9] "Lockheed Martin Awarded $25M U.S. Navy Contract for TB-37X Multi-Function Towed Array (MFTA) System," Defpost, 21 September 2019. [Online]. Available: https://defpost.com/lockheed-martin-awarded-25m-u-s-navy-contract-for-tb-37x-multi-function-towed-array-mfta-system/.

[10] M. Gilday, "America's Navy CNO FRAGO 01/2019," December 2019. [Online]. Available: https://media.defense.gov/2020/Jul/23/2002463491/-1/-1/1/CNO%20FRAGO%2001_2019.PDF.

[11] J. Barhen, "Sensor Data Processing for Tracking Underwater Threats Using Terascale Optical Core Devices," in *Advances and Challenges in Multisensor Data and Information Processing*, Amsterdam, Netherlands, IOS Press, Incorporated, 2007, pp. 267–282.

[12] F. Fahy, “Measurement of acoustic intensity using the cross-spectral density of two microphone signals,” *The Journal of the Acoustical Society of America,* vol. 62, no. 4, pp. 1057–1959, 1977, doi: 10.1121/1.381601.

[13] Naval Sea Systems Command, “NUWC Division Newport,” 17 September 2015. [Online]. Available: https://www.navsea.navy.mil/Portals/103/Documents/NUWC_Newport/Reading Room/Code15BBTPConference.pdf. [Accessed 28 October 2020].

[14] J. Hlavin, “Hydrostatic and Hydrodynamic Analysis of a Lengthened DDG-51 Destroyer Modified Repeat,” M.S. thesis, Dept. of Mech. and Aerospace Eng., NPS, Monterey, CA, USA, 2010 [Online]. Available: http://hdl.handle.net/10945/5287.

[15] Congressional Research Service, “Navy Ship Acquisition: Options for Lower-Cost Ship Designs--Issues for Congress,” Congressional Research Service, Washington, DC, USA, CRS Report No. RL32914, 2016.

[16] F. Fahy, *Sound Intensity,* London, UK, Spon Press, 1995.

[17] G. Karunasiri, “Fabrication of MEMS Direction Acoustic Sensors for Underwater Operation,” *Sensors (Basel, Switzerland),* vol. 20, no. 5, pp. 1245-, Feb 2020, doi: 10.3390/s20051245.

[18] US Department of Defense, “Unmaned Systems Integrated Roadmap,” Washington, DC, USA, 2018. [Online]. Available: https://news.usni.org/2018/08/30/pentagon-unmanned-systems-integrated-roadmap-2017-2042.

[19] RAND National Defense Research Institute, “A Survey of Missions for Unmanned Undersea Vehicles,” RAND Corporation, Santa Monica, CA, USA, 2009. [Online]. Available: https://www.rand.org/pubs/monographs/MG808.html.

[20] M. Dossot, “An investigation of the capabilities of a short hydrophone array towed by an ocean glider,” *The Journal of the Acoustical Society of America,* vol. 122, no. 5, pp. 3009-, 2007, doi: 10.1121/1.2942749..

[21] U.S. Navy, “Fact File MH-60 Sea Hawk Helicopter,” 6 Feburary 2020. [Online]. Available: https://www.navy.mil/Resources/Fact-Files/Display-FactFiles/Article/2166650/mh-60-sea-hawk-helicopter/.

[22] T. Emmersen et al., “Advanced Undersea Warfare Systems,” Dept. of Sys. Eng., NPS, Monterey, CA, USA, 2011. [Online]. Available: http://hdl.handle.net/10945/6959.

[23] B. B. Bauer and A. DiMattia, “Moving-Coil Pressure-Gradient Hydrophone,” *The Journal of the Acoustical Society of America*, vol. 39, no. 6, p. 1264–1264, Jun. 1966, doi: 10.1121/1.1942933.

[24] Olson, H. F., “A Unidirectional Microphone,” *Journal of the Society of Motion Picture Engineers*, vol. 27, no. 3, p. 284–301, Sep. 1936, doi: 10.5594/J01272.

[25] I. Wolff and F. Massa, “Use of pressure gradient microphones for acoustical measurements,” *The Journal of the Acoustical Society of America*, vol. 4, no. 3, pp. 217–234, Jan. 1933, doi: 10.1121/1.1915602.

[26] C. B. Leslie, J. M. Kendall, and J. L. Jones, “Hydrophone for Measuring Particle Velocity,” *The Journal of the Acoustical Society of America*, vol. 28, no. 4, pp. 711–714, Jul. 1956, doi: 10.1121/1.1908455.

[27] T. B. Gabrielson, D. L. Gardner, and S. L. Garret, “A simple neutrally buoyant sensor for direct measurement of particle velocity and intensity in water,” *The Journal of the Acoustical Society of America*, vol. 97, no. 4, pp. 2227–2237, Apr. 1995. doi: 10.1121/1.411948.

[28] M. A. Josserand and C. Maerfeld, “PVF2 velocity hydrophones,” *The Journal of the Acoustical Society of America*, vol. 78, no. 3, p. 861–867, Sep. 1985, doi: 10.1121/1.392916.

[29] H. K. Rockstad, T. W. Kenny, P. J. Kelly, and T. B. Gabrielson, “A microfabricated electrontunneling accelerometer as a directional underwater acoustic sensor,” in *American Institute of Physics*, Mystic, Connecticut, 1996, vol. 368, pp. 57–68. doi: 10.1063/1.50357.

[30] M. B. Moffett, D. H. Trivett, P. J. Klippel, and P. D. Baird, “A piezoelectric, flexural-disk, neutrally buoyant, underwater accelerometer,” *IEEE Trans. Ultrason., Ferroelect., Freq. Contr.*, vol. 45, no. 5, p. 1341–1346, Sep. 1998, doi: 10.1109/58.726460.

[31] K. Kim, T. B. Gabrielson, and G. C. Lauchle, “Development of an accelerometer-based underwater acoustic intensity sensor,” *The Journal of the Acoustical Society of America*, vol. 116, no. 6, p. 3384–3392, 2004. doi:10.1121/1.1804632.

[32] K. Kim, G. C. Lauchle, and T. B. Gabrielson, “Near-field acoustic intensity measurements using an accelerometer-based underwater intensity vector sensor,” *Journal of Sound and Vibration*, vol. 309, no. 1, pp. 293–306, Jan. 2008, doi: 10.1016/j.jsv.2007.0.

[33] U. K. Chandrika and V. N. Hari, “A vector sensing scheme for underwater acoustics based on particle velocity measurements,” in *in OCEANS 2015 - MTS/IEEE Washington*, Washington, DC, Oct. 2015, pp. 1–7, doi: 10.23919/OCEANS.2015.7404533.

[34] Bahreyni et al., “A Wideband, Low-Noise Accelerometer for Sonar Wave Detection,” *IEEE Sensors J.*, vol. 18, no. 2, pp. 508–516, Jan. 2018, doi: 10.1109/JSEN.2017.2774705.

[35] J. Choi, J. Park, Y. Lee, J. Jung, and H.-T. Choi, “Robust Directional Angle Estimation of Underwater Acoustic Sources Using a Marine Vehicle,” *Sensors*, vol. 18, no. 9, p. 3062, Sep. 2018, doi: 10.3390/s18093062.

[36] Y. Roh, S. Pyo, and S. Lee, “Design of an accelerometer to maximize the performance of vector hydrophones,” in *SPIE*, Denver, Mar. 2018, doi: 10.1117/12.2295910.

[37] W. Zhang, L. Guan, G. Zhang, C. Xue, K. Zhang, and J. Wang, “Research of DOA Estimation Based on Single MEMS Vector Hydrophone,” *Sensors*, vol. 9, no. 9, p. 6823–6834, Aug. 2009, doi: 10.3390/s90906823.

[38] H. Zhang, H. Chen and W. Wang, “An Underwater Acoustic Vector Sensor with High Sensitivity and Broad Band,” *Sensors & transducers*, vol. 170, no. 5, p. 30-34, May 2014.

[39] S. Liu, Y. Lan, and T. Zhou, “Theory and design of acoustic dyadic sensor,” *in 2016 IEEE/OES China Ocean Acoustics (COA), Harbin*, p. 1-5, Jan. 2016. doi: 10.1109/COA.2016.7535634.

[40] R. N. Miles, D. Robert, and R. R. Hoy, “Mechanically coupled ears for directional hearing in the parasitoid fly Ormia ochracea,” The Journal of the Acoustical Society of America,,” vol. 98, no. 6, p. 3059–3070, Dec. 1995, doi: 10.1121/1.413830.

[41] D. Wilmott, F. Alves, and G. Karunasiri., “Bio-inspired miniature direction finding acoustic sensor,” Sci. Rep. vol. 6, 29957, Jun. 2016. [Online]. doi: 10.1038/srep29957.

[42] G. E. Da Re, “MEMS underwater direction finding acoustic sensor,” M.S. thesis, Dept. of Physics, NPS, Monterey, CA, USA, unpublished.

[43] J. D. Collins, “Bio-Inspired MEMS Direction Finding Underwater Acoustic Sensor,” M.S. thesis, Dept. of Physics, NPS, Monterey, CA, USA 2017. [Online]. Available: http://hdl.handle.net/10945/63794.

[44] W. D. Swan, “Bio-inspired MEMS direction finding acoustic sensor for air and underwater applications,” M.S. thesis, Dept. of Physics, NPS, Monterey, CA, USA, unpublished..

[45] A. Espinoza, “Packaging and characterization of Bio-inspired MEMS underwater MEMS directional sound sensor,” M.S. thesis, Dept. of Physics, NPS, Monterey, CA, USA, unpublished.

[46] Brigham Young University Department of Physics, “Wave Propagation,” Acoustics Research Group, [Online]. Available: https://acoustics.byu.edu/animations-propagation. [Accessed 28 October 2020].

[47] J. W. S. Rayleigh, *The Theory of Sound, Volume 1,* London, UK, Macmillan and Company, 1877.

[48] C. Liu, *Foundations of MEMS,* Upper Saddle River, NJ, USA, Prentice Hall Press, 2011, doi: 10.5555/2011937.

[49] R. N. Miles and R. R. Hoy, “The Development of a Biologically-Inspired Directional Microphone for Hearing Aids,” *Audiol Neurotol,* vol. 11, no. 2, p. 86-94, 2006. doi: 10.1159/000090681.

[50] R.N. Miles et al., “A low-noise differential microphone inspired by the ears of the parasitic fly Ormia ochracea,” *The Journal of the Acoustical Society of America,,* vol. 125, no. 4, p. 2013–2026, Apr. 2009. doi: 10.1121/1.3082118.

[51] Endevco, “Instruction Manual for Model 22, Picomin Accelerometer,” [Online]. Available: https://buy.endevco.com/accelerometer/22-accelerometer. [Accessed 27 October 2020].

[52] PCB Piezotronics, “Model 356A33 Installation and Operating Manual,” [Online]. Available: https://www.pcb.com/products?model=356a33. [Accessed 27 October 2020].

[53] S. Touse, “Fabrication of a microelectromechanical directional sound sensorwith electronic readout using comb fingers,” Applied Physics Letters, vol. 96, no. 17, pp. 173701–173701–3, Apr. 2010, doi: 10.1063/1.3418640..

[54] S. Ljunggren, “Sound reduction of a double-wall cylinder at discrete angles of incidence,” *Acousitca,* vol. 63, no. 3, pp. 229–231, May 1987.

[55] E. Szechenyi, “Sound transmission through cylinder walls using statistical considerations,” *Journal of sound and vibration,* vol. 19, no. 1, pp. 83–94, 1971.

[56] P. Oliazadeh, A. Farshidianfar, and M. J. Crocker, “Experimental and analytical investigation on sound transmission loss of cylindrical shells with absorbing material,” *Journal of Sound and Vibration,* vol. vol. 434, p. 28-43, Nov. 2018, doi: 10.1016/j.jsv.201.

[57] L.R. Koval, “Effects of cavity resonance on sound transmission into a cylindrical shell,” *Journal of sound and vibration,* vol. 59, no. 1, pp. 22–33, 1978.

[58] R. Rabelo, private communication, Nov. 2020.

[59] Acoustical Society of America, *Acoustical Terminology,* New York, NY, USA: American Standards Association, Inc., 1951.

[60] Endevco, “2775A Signal conditioner Instruction manual,” Endevco, [Online]. Available: https://www.endevco.com/service-and-support/legacy-products. [Accessed 27 10 2020].

INITIAL DISTRIBUTION LIST

1. Defense Technical Information Center
   Ft. Belvoir, Virginia

2. Dudley Knox Library
   Naval Postgraduate School
   Monterey, California